https://doi.org/10.5194/se-2021-17
Preprint. Discussion started: 25 February 2021

Solid Earth
Discussions

Contribution of gravity gliding in salt-bearing rift basins – A new experimental setup for simulating salt tectonics under the influence of sub-salt extension and tilting

Michael Warsitzka[1], Prokop Závada[1], Fabian Jähne-Klingberg[2], and Piotr Krzywiec[3]

[1]Institute of Geophysics of the Czech Academy of Sciences, Boční II/1401, 14131 Praha, Czech Republic
[2]Federal Institute for Geosciences and Natural Resources, Stilleweg 2, 30655 Hannover, Germany
[3]Institute of Geological Sciences, Polish Academy of Sciences, Twarda 51/55, 00-818 Warsaw, Poland

Correspondence: Michael Warsitzka (warsitzka@ig.cas.cz)

Abstract. Basin-scale salt flow and the evolution of salt structures in rift basin is mainly driven by sub- and supra-salt faulting and sedimentary loading. Crustal extension is often accompanied and followed by thermal subsidence leading to tilting of the graben flanks, which might induce an additional basinward directed driver for salt tectonics. We designed a new experimental analog apparatus capable of integrating the processes of sub-salt graben extension and tilting of the flanks, such that the overlapping effects on the deformation of a viscous substratum and the brittle overburden can be simulated. The presented experimental study was performed to demonstrate the main functionality of the experimental procedure and setup demonstrating the main differences in structural evolution between conditions of pure extension, pure tilting and extension combined with tilting. Digital image correlation of top view stereoscopic images was applied to reveal the 3D displacement and strain patterns. Results of these experiments suggest that in salt basins affected by sub-salt extension and flank inclination, the salt flow and downward movement of overburden affects the entire flanks of the basin. Supra-salt extension occurring close to the graben centre is overprinted by the downward movement, i.e. amount of extension is reduced or extensional faults zones are shortened. At the basin margins, thin-skinned extensional fault developed, which resemble fault zones observed on basin flanks offset from the central graben zone.

1 Introduction

Salt layers in sedimentary basins play a key role in the structural and sedimentary evolution. As the bulk mechanical behavior of rock salt on a geological time scale is that of a viscous fluid, it is able to flow in response to an internal pressure gradient and external shear forces (Jackson and Hudec, 2017). Salt flow is mainly driven by two factors (Jackson and Hudec, 2017): (1) differential loading due to lateral differences in thickness and density of the suprasalt overburden (e.g. deltaic progradation, minibasin subsidence etc.) can trigger widespread squeezing of the salt and vertical collapse and lateral expansion of the overburden ('gravity spreading'; Schultz-Ela (2001)), and (2) any vertical displacement (e.g. tilting of the salt layer) that can cause gravitational downward salt flow and, under some circumstances, gravitational collapse of overburden strata ('gravity gliding'; Schultz-Ela (2001)).

Driving processes of salt flow are well explained for salt-bearing passive margin basins, e.g. Lower Congo Basin, Western Mediterranean and the Santos Basin (Fort et al., 2004; Quirk et al., 2012; Jackson et al., 2015; Mianaekere and Adam, 2020), where both driving factors mostly act in the same seaward direction (Fig. 1a) (e.g. Brun and Fort, 2011; Peel, 2014). Scaled laboratory experiments focusing on passive margin salt tectonics reveal that seaward directed tilting of the basin floor and/or sediment progradation typically cause the formation of a downdip compressional and an updip extensional domain (Fig. 1a) (e.g. Jackson and Cramez, 1989; Mauduit et al., 1997; Brun and Mauduit, 2009; Brun and Fort, 2011; Ge et al., 2019). The initiation of gravity gliding and spreading depends on the angle of the basin slope and of the top surface (e.g. Vendeville, 2005; Rowan et al., 2012), i.e. the gravitational potential has to be sufficient to overcome the compressional, frictional strength of the overburden strata at the foot of the slope (Rowan et al., 2004).

In salt-bearing rift basins (SBRB), these driving forces act oppositely (Fig. 1b). On one side, the sedimentary regime in SBRB is commonly characterized by aggradation with maximum sediment thickness in the basin centre and less sedimentation or erosion at the basin margins. In many SBRB, such as the Glückstadt Graben, the Central Graben and the Polish Basin (Penge et al., 1999; Stewart, 2007; Krzywiec, 2004), salt is almost completely evacuated from the basin centre towards diapirs on the basin flanks, whereas the graben centre is filled up with several kilometers of syn-kinematic sediments (Krzywiec, 2004; Maystrenko et al., 2005; Warsitzka et al., 2017). This evacuation was likely driven by upward directed gravity spreading due to sedimentary loading (Hudec and Jackson, 2007; Warsitzka et al., 2018). Conversely, the graben flanks are often inclined towards a basin centre mainly due to thermal subsidence and flexural loading (e.g. Buchanan et al., 1996) causing basinward directed stresses. Downward gravity gliding is often inferred from the occurrence of a domain of thin-skinned extensional structures at the upslope basin margin (e.g. Penge et al., 1999; Geil, 1991; Stewart and Coward, 1995; Best, 1996; Withjack and Callaway, 2000; Thieme and Rockenbauch, 2001; Mohr et al., 2005; Tvedt et al., 2013; Vackiner et al., 2013; Labaume and Teixell, 2020). For instance, in the northern Central Graben (central North Sea) and the Sole Pit Basin (southwestern North Sea) (e.g. Hughes and Davison, 1993; Coward and Stewart, 1995; Stewart and Coward, 1995), thin-skinned rollovers and separated blocks ('rafts') are observed above the tilted outer platforms of the rift basins (Hodgson et al., 1992; Buchanan et al., 1996; Penge et al., 1999). It is suggested that these structures formed by a combination of gravitationally and tectonically driven extension ('rift-raft tectonics') (Stewart and Clark, 1999; Penge et al., 1999) and, in some cases, coincided with thin-skinned shortening in the basin centre (e.g. Hughes and Davison, 1993; Coward and Stewart, 1995; Stewart and Coward, 1995). Thus, it is unclear to date how gravity gliding can take place during sediment aggradation in the basin centre, because thick overburden sediments may act as resisting buttress against gravity gliding. The oppositely acting processes of gravity spreading and gliding in SBRB provoke the question, which geological configurations have to be fulfilled to initiate gravity gliding in SBRB, i.e. which minimum topographic gradient and basin slope is required? Furthermore, it is unclear, how gravity gliding affects basin-wide salt flow and the evolution of salt structures in SBRB and which driving process prevail at what period of the basin evolution.

Analog models dedicated to the opposing interplay between gliding and spreading in SBRB show that salt flows downward if the depocentre above the downthrown block is underfilled and returns to upward directed flow as soon as syn-kinematic sediments are accumulated in the depocentre (e.g. Vendeville et al., 1995; Koyi et al., 1993; Ge et al., 1997; Dooley et al., 2005; Burliga et al., 2012; Warsitzka et al., 2015; Lymer et al., 2018; Dooley and Hudec, 2020). Basin-scale models reproduced thin-skinned extensional structures occurring on the flanks of the graben resulting from the decoupling effect of the salt layer (Nalpas and Brun, 1993; Koyi et al., 1993; Dooley et al., 2005; Ferrer et al., 2014; Moragas et al., 2017). Other experiments demonstrated how progradation of sedimentary wedges across extensional systems modify sedimentary patterns in the overburden by introducing an additional component of gravity spreading (Loncke et al., 2010; Rojo et al., 2020). However, the influence of basin-wide tilting of the subsalt basement and, hence, effects of gravity gliding, on the evolution of supra-salt sedimentary structures and salt flow pattern have not been investigated yet.

The key motivation of this project is to evaluate the influence of regional scale gravity gliding on salt flow processes and the initiation of minibasins in SBRB. We designed a new apparatus for analog modeling to integrate the simulation of crustal scale extension and tilting of the graben flanks. Here, the basic concept of the apparatus and results of preliminary experiments is presented. Based on the techniques of digital image correlation, we compare displacement and strain patterns between different scenarios: (1) only extension, (2) only tilting of the flanks, (3) combined extension and tilting and (4) extension, tilting and syn-kinematic sedimentation. In order to demonstrate the effect of the presence of a viscous detachment, these scenarios were performed with and without a viscous substratum. The experimental results illustratively demonstrate the functionality of the apparatus and reveal first main differences between rift basins with tilted flanks and those surrounded by flat flanks.

2 Geological prototype and experimental setup

The experimental setup and the procedure are inspired by a generalized natural salt-bearing rift basin (Fig. 1c). Boundary conditions and basin configurations, such as width of the basin, maximal amount of tilting, extension rate, layer thicknesses and timing of extension, were derived from a survey of various SBRB worldwide (Tab. 1). In most basins, the initial phase of rifting occurred prior to deposition of the major salt layer and in some case continued during deposition. The early post-salt evolution ($\sim$ 10 to 20 Ma after salt deposition) is usually characterized by multiple phases of rifting each followed by post-rift thermal subsidence. Thermal relaxation and sedimentary loading usually cause subsidence in a wider region compared to that of the stretched extensional graben (Watts et al., 1982). We assume that these subsidence processes are the main drivers for the tilting of the graben flanks. Such tilting can be as much as 10° (4.5° in average) over a length of up to 100 km (60 km in average; Tab. 1). The supposed maximal thickness of the original salt layer in the basin centre ranges between 800 and 4000 m (1800 m in average), but pinches out towards the basin margins. The pre-kinematic layer is defined as the post-salt overburden deposited prior to the first post-salt extensional phase. In some basins, the thickness of this layer is probably 0 ($\sim$450 m in average), because syn-salt rifting continued after end of salt deposition. The lithology of the pre-kinematic overburden can be fine- or coarse-grained clastics or carbonates. Therefore, we assume an averaged lithological composition when relating physical properties between model and nature (see below).

Table 1. Literature-based data compilation of worldwide salt-bearing rift basins. The thickness of the salt layer refers to the estimated maximum thickness of the original evaporitic layer. The pre-kinematic layer is defined as the sedimentary layer accumulated after the salt deposition and before the first post-salt rifting phase. * denotes basins in which gravity-driven salt tectonics has been proposed or proofed.

Basin	Age of salt layer	Pre- & syn-salt rifting	Post-salt rifting	Thickness salt [m]	Thickness prekin. cover [m]	Max. offset subsalt faults	Tilting of flanks [$^\circ$]	Width of flanks [km]	References
Arzacq-Mauleon Basin*	Late Triassic	Late Permian–Early Triassic	Late Jurassic	2700	1000	4000	9	80	Lagabrielle et al. (2010); Saspiturry et al. (2019); Labaume and Teixell (2020)
Atlas Basin	Late Triassic	Late Permian–Late Triassic	Early Jurassic	1500	100	3500	3	100	Martín-Martín et al. (2017); Moragas et al. (2017); Troudi et al. (2017); Vergés et al. (2017)
Basque-Cantabrian Basin*	Late Triassic	Late Permian–Early Triassic	Late Jurassic	2700	500	3000	6	75	Bodego and Agirrezabala (2013); López-Mir et al. (2015); Saura et al. (2016); Cámara (2020)
Central Graben (North)*	Late Permian	Early Permian	Early–Mid Triassic	2000	1000	1000	5	90	Hodgson et al. (1992); Høiland et al. (1993); Buchanan et al. (1996); Penge et al. (1999); Duffy et al. (2013)
Central Graben (central)	Late Permian	Early Permian	Mid Triassic	1500	1000	1000	2	20	Tanveer and Korstgård (2009); Ge et al. (2017)
Central Graben (south)	Late Permian	Early Permian	Early Triassic	1500	300	3000	3	40	Geluk (2005); Wong et al. (2007); Van Winden et al. (2018)
Dniepr-Donets Basin	Late Devonian	Late Devonian	Early Carboniferous	2000	300	5000	6	600	Kusznir et al. (1996); Stovba et al. (1996); Stovba and Stephenson (2003)
East Texas Basin*	Mid Jurassic	Triassic	mid Upper Jurassic	800	600	1000	4.5	60	Seni and Jackson (1984)
Egersund Basin*	Late Permian	Permian	Mid Triassic	800	700	2500	5.5	40	Lewis et al. (2013); Tvedt et al. (2016); Jackson and Lewis (2016); Ge et al. (2017)
Ems Trough*	Late Permian	Permian	Mid Early Triassic	900	300	600	2.5	70	Radies et al. (2005); Baldschuhn et al. (2001); Strozyk et al. (2017)
Forth Approaches Basin*	Late Permian	Early Permian	Late Permian	600	0		2	35	Clark et al. (1998); Stewart and Clark (1999); Cartwright et al. (2001); Stewart (2007)
Glückstadt Graben	Permian	Early Permian	Early Triassic	3000	800	4000	5	50	Maystrenko et al. (2005, 2017); Warsitzka et al. (2017)
Halten Terrace	Mid–Late Triassic	Late Permian–Early Triassic	Mid Jurassic	1000	1200	2000	4	80	Pascoe et al. (1999); Dooley et al. (2003); Coleman et al. (2017)
Horn Graben*	Late Permian	Permian	Early Triassic	1500	400	4000	5	50	Vejbæk (1990); Best et al. (1983); Kockel et al. (1995)
Lauwerszee Trough*	Late Permian	Permian	Late Permian	1400	0	1000	3	50	Van Gent et al. (2011); Strozyk et al. (2014)
Lusitanian Basin	Late Triassic–Early Jurassic	Late Triassic	Early Jurassic	1500	0	2000	5	40	Rasmussen et al. (1998); Alves et al. (2002); Pena dos Reis et al. (2017)
Nordkapp Basin	Late Carboniferous	Late Devonian–Late Carboniferous	Late Permian	4000	800	2000	3	55	Jensen and Sørensen (1992); Koyi et al. (1995); Nilsen et al. (1996); Rowan and Lindsø (2017); Rojo et al. (2019)
Norwegian-Danish Basin	Late Permian	Early Permian	Late Triassic–Early Jurassic	1500	300	3000	5	80	Vejbæk (1990); Geil (1991); Clausen and Pedersen (1999)
Parentis Trough*	Late Triassic	Late Permian–Early Triassic	Late Jurassic	1000	1000	4000	10	30	Ferrer et al. (2008); Jammes et al. (2009, 2010); Ferrer et al. (2012)
Polish Basin	Late Permian	Late Permian	Early–Mid Triassic	2500	0	3500	7	80	Dadlez et al. (1995); Wagner et al. (2002); Krzywiec (2004); Krzywiec et al. (2017)
Red Sea Basin*	Mid Miocene	Oligocene	Late Miocene	2000	0	1000	7	40	Mitchell et al. (1992); Heaton et al. (1995)
Slyne Trough*	Late Permian	-	Late Triassic	300	200	2000	5	20	Dancer et al. (1999)
Sole Pit Trough*	Late Permian	–	Late Triassic	1500	600	500	2.5	90	Walker and Cooper (1987); Hughes and Davison (1993); Stewart and Coward (1995)
Western Approaches Basin	Late Triassic	Early–Mid Triassic	Mid Jurassic	1100	0	3000	∼4.5	30000	Chapman (1989)
Average	-	-	-	∼1500	∼400	∼2200	∼4.5	60000	
Scaled model parameters	-	-	-	0.016	0.006	0.022	4	0.6	

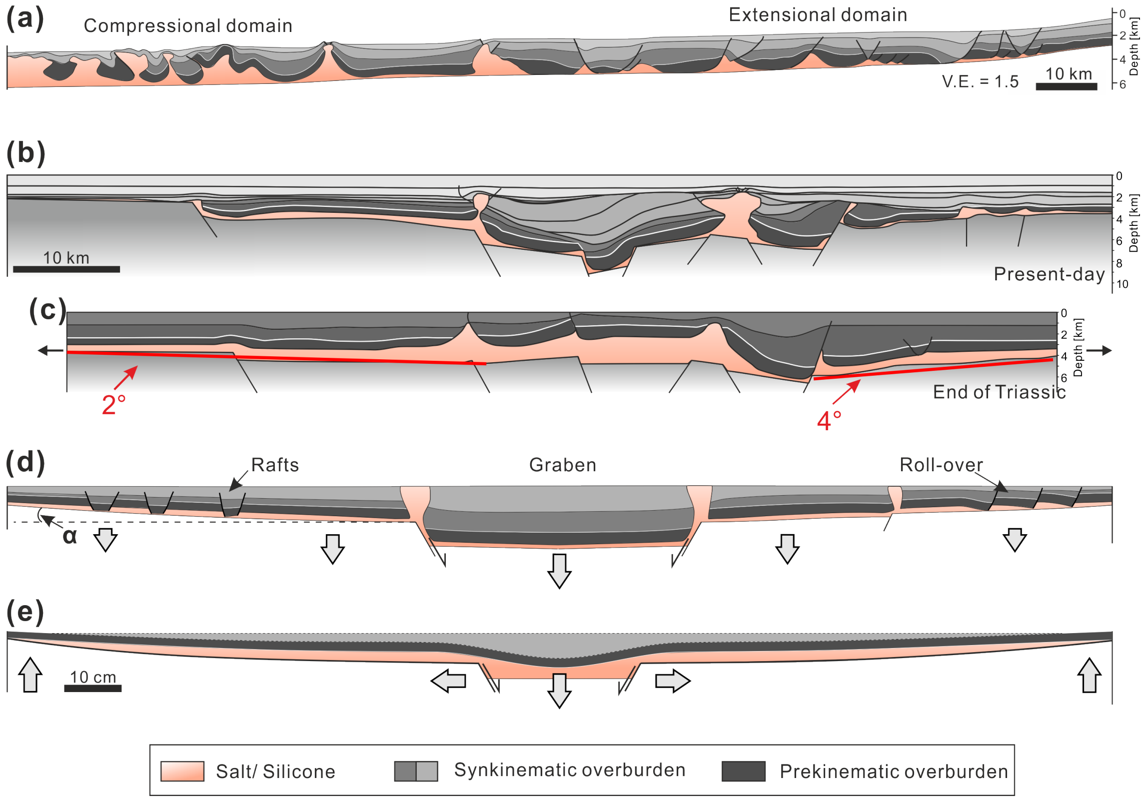

Figure 1. (**a**) Geological cross section of the Angolan passive margin, where basinward directed gravity gliding and spreading lead to the formation of an upslope extensional and a downslope compressional domain (Fort et al., 2004). (**b**) Geological cross section of the Central Graben (North Sea) (Van Winden et al., 2018). Diapirs and other salt-related structures develop due to sub- and supra-salt extension. (**c**) Restored cross section of (b) to the top Upper Triassic showing inclined flanks of the rift basin. Note that redistribution of the salt was included in the restoration procedure by Van Winden et al. (2018). However, restored thickness of Triassic layers and estimates of the original salt layer thickness (Ten Veen et al., 2012) provide reasonable implications for the geometry of the sub-salt base. (**d**) Schematic cross section showing structures typically observed in SBRB, such as thin-skinned extensional "rafts" and rollovers on the graben flanks and as well as dapirs and minibasins in the centre. (**e**) Concept of the experimental setup applied in the presented study. Graben extension is simulated by a vertically moving central block and two laterally moving flanks. Tilting of the flank (due to thermal subsidence) is modeled by an upward bending of the outer margins.

3 Method

3.1 Experimental setup

The experimental apparatus consists of a ∼30 cm wide graben structure in the centre, which can be moved vertically (Fig. 2a). The graben flanks are made of bendable plates (∼100 cm), which are pushed outward by the down-going central block to simulate tectonic extension. Independent from the lateral movement, the outer edges of the flanks can be uplifted so that the plates are bent and inclined. Thermal subsidence in nature leads to widespread, saucer-shaped subsidence of the basin. However, the net effect of thermal subsidence is differential vertical movement between the graben centre and the flanks, which is here mimicked by an uplift of the flanks. The depth (y-axis) of the plates is roughly 60 cm, which is sufficient to reduce boundary effects at the confining lateral sand walls (Fig. 2b).

The experimental surface is recorded by 2 stereoscopic CMOS sensor cameras ('Imager M-lite 12M camera', 12-bit monochrome, 12 MPx resolution) in top view to analyse the evolution of the surface displacements and strains (Adam et al., 2005). Images are acquired and processed by the StrainMaster© (LaVision GmbH) 3D digital image correlation (DIC) software (Adam et al., 2005; LaVision, 2018). The 3D-DIC analysis is an optical, non-intrusive method to determine shapes, displacement and deformation in high sub-millimeter resolution.

3.2 Experimental materials

The viscous behavior of salt (e.g. Urai et al., 2008) is simulated by a silicone putty (Polydimethylsiloxane, PDMS; Rudolf et al. (2015)) sold under the name Korasilon G 20 OH (Kurt Obermeier GmbH & Co. KG). The viscosity of the silicone was measured in the analog laboratory of the Helmholtz Centre Potsdam GFZ German Research Centre for Geosciences using a cone-plate rheometer (RC20.1-CPS-P1, RheoTec). The dynamic viscosity is 2.2–2.8$\times10^4$ Pas, which is slightly temperature-dependent (decrease of 1.4–1.9 % per 1 K increase), and the density is 970 kgm^{-3} at 25°C. It has a Newtonian behavior at low strain rates ($<10^{-2}$) and a strain rate softening behavior above relatively high strain rates ($>10^{-2}$ s^{-1}) (Rudolf et al., 2016).

Frictional-plastic behavior of overburden sediments is modeled by granular mixtures of quartz (bulk density = 1620 kgm^{-3}) sand and silicate cenospheres (bulk density = 430 kgm^{-3}) with various mixing ratios. In order to adapt the density ratio between the ductile silicone and the overburden sand to match the natural density ratio (see below), various mixtures of both granulates were used. Similar to upper crustal rocks, such granulates deform according to the Mohr–Coulomb failure criterion (Equ. 3; (e.g. Lohrmann et al., 2003; Panien et al., 2006)). Frictional properties (coefficient of internal friction μ, cohesion C; Tab. 2) and densities of the mixtures were determined in ring shear tests in the laboratory of the Helmholtz Centre Potsdam GFZ German Research Centre for Geosciences. Details of the measurements and the material properties can be found in Warsitzka et al. (2019).

3.3 Scaling

For the analog model to be representative of the natural prototype, models have to be geometrically, dynamically, kinematically and rheologically similar to their natural prototype (Hubbert, 1937; Ramberg, 1981; Weijermars and Schmeling, 1986; Davy and Cobbold, 1991; Weijermars et al., 1993; Bonini et al., 2012). In the presented models, we simulated the deformation processes of tectonically driven extension and gravity driven gliding and spreading and identified the following characteristic parameters describing the boundary conditions of these processes (cf. Fig. 3): layer thickness (h_b, h_d), densities (ρ_b, ρ_d), cohesion and coefficient of internal friction of the brittle overburden (C, μ), viscosity of the ductile layer (η), extension rate (u_e) and tilting rate (u_t). Extension and tilting rates depend on the geometrical and kinematical scaling and determine the amount of extension and tilting during experimental time.

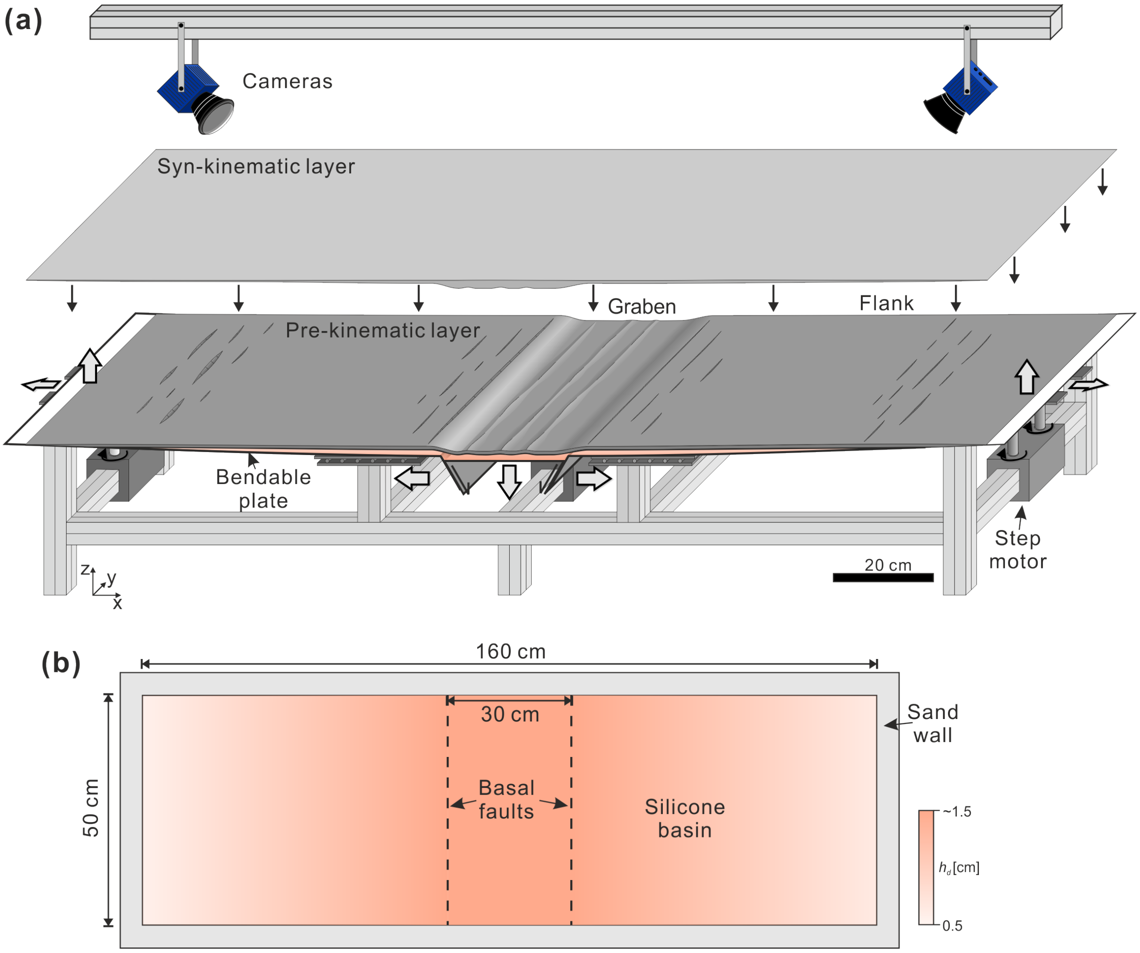

Figure 2. (**a**) Sketch of the experimental setup. The apparatus consists of a central, vertically moving graben structure bounded by two bendable metal plates. The latter can be moved laterally and their outer edges can be uplifted. All parts can be controlled separately. The experimental surface is monitored by 2 stereoscopic cameras from above and images are utilized for 3D digital image correlation (Adam et al., 2005). (**b**) Top view sketch of the silicone basin displaying the thickness distribution of the silicone layer. The basin is confined by sand walls, which are not shown in a.

Geometric scaling ensures that corresponding ratios of lengths and angles are comparable between model and nature. The choice of the geometrical scaling ratio is determined by the procedure for dynamical scaling (Pollard et al., 2005) and, in our study, similar to previous model studies (e.g. Vendeville et al., 1995; Koyi et al., 1993; Warsitzka et al., 2015; Dooley and Hudec, 2020):

130 $$\frac{L_m}{L_n} = 10^{-5} \quad (1)$$

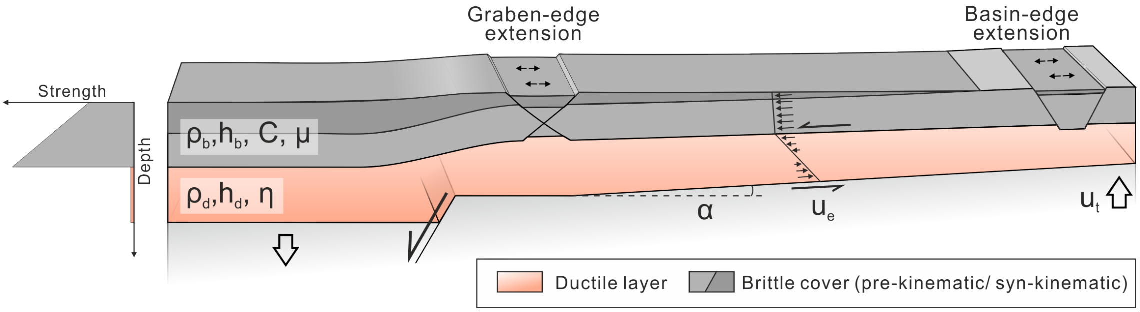

Figure 3. Physical parameters describing the deformation processes in the experiments. Lateral displacement due to basal extension and downward gliding of the overburden lead to shearing at the base and the top of viscous layer. Vertical displacement of the graben block and the flanks cause gravitational instability in the viscous layer. Syn-kinematic sedimentation, i.e. filling the subsided depocentres, imposes differential loading on top of the viscous layer. Governing parameters describing these processes are: h_b – thickness of the brittle overburden, h_d – thickness of the ductile substratum, η – dynamic viscosity of the ductile material, μ – Coefficient of internal friction, C – cohesion, u_e – extension rate, u_t – uplift rate, α – tilt angle of the basin flank

.

This means that 1 cm in the model represents 1 km in nature and characteristic geometrical relationships, such as the thickness ratio between overburden and salt or the ratio between extensional displacement and flank uplift can be scaled accordingly (Tab. 1).

Fundamental principles of dynamical scaling require that trajectories and ratios of forces acting on the material have to be equal and that rheological behaviors of the involved materials are similar (Weijermars and Schmeling, 1986; Pollard et al., 2005). This can be translated to the concept that driving and resisting forces of the relevant processes have to be related properly. In salt tectonics, driving forces are produced by (1) vertical loading of sediments resulting in a gravitational buoyancy forces, and by (2) tectonic stresses resulting in lateral pressure forces (Jackson and Hudec, 2017). Resisting forces are caused by (1) the frictional strength of the brittle overburden (S_F), and by (2) viscous stresses in the ductile layer (S_V) caused by drag at its boundaries (Jackson and Hudec, 2017). Inertial forces can be considered as insignificant, since strain rates during solid rock flow are very low (Ramberg, 1981; Weijermars and Schmeling, 1986).

Because deformation style and localization in the materials is mostly influenced by rheological parameters of the ductile layer and its brittle overburden, a characteristic measure for dynamical scaling is the brittle-to-ductile strength ratio or 'Brittle-ductile-coupling' (BDC) (e.g. Sornette et al., 1993; Schueller and Davy, 2008). This is calculated by integrating the differential stress over the layer thicknesses (Schueller and Davy, 2008):

$$BDC = \frac{F_F}{F_V} = \frac{\int_0^{h_b}(\sigma_1 - \sigma_3)dz}{\int_0^{h_d}(\sigma_1 - \sigma_3)dz} \tag{2}$$

The frictional strength of both, brittle sediments and experimental granular materials, obeys the Mohr-Coulomb criterion according to which the mean stress σ_m and the maximum shear stress τ_{max} are related by (Byerlee, 1978; Dahlen, 1990; Jaeger et al., 2007):

$$\tau_{max} = \sigma_m sin\phi + Ccos\phi \tag{3}$$

Here, ϕ is the angle of internal friction and C the cohesion. Translated to an expression by the maximum and the minimum principal stresses σ_1 and σ_3 gives:

$$\frac{\sigma_1 - \sigma_3}{2} = \frac{\sigma_1 + \sigma_3}{2} sin\phi + Ccos\phi \tag{4}$$

In an extensional stress field, the maximal principal stress σ_1 equals the lithostatic pressure σ_L:

$$\sigma_1 = \sigma_{zz} = \rho_b g h_b \tag{5}$$

where g is the gravitational acceleration and ρ_b the density of the brittle overburden. Furthermore, the minimal principal stress σ_3 is horizontal:

$$\sigma_3 = \sigma_{xx} \tag{6}$$

With the presence of a pore fluid pressure, each pressure has to be corrected by the pore fluid pressure ratio (Hubbert-Rubey coefficient of fluid pressure λ) (Weijermars et al., 1993):

$$\sigma' = \sigma(1-\lambda) \tag{7}$$

Assuming that pore fluid pressure is hydrostatic, λ becomes roughly 0.45 for an average overburden density of 2200 kg m^{-3} and a fluid density of 1050 kg m^{-3}. The critical horizontal stress at failure (Dahlen, 1990):

$$\sigma_{xx} = \sigma'_{zz}\frac{1-sin\phi}{1+sin\phi} - 2C\sqrt{\frac{1-sin\phi}{1+sin\phi}} \tag{8}$$

Combining Eq. (4), (5) and (8) gives the brittle strength in a tensional stress regime: (Weijermars et al., 1993):

$$S_F = \rho_b g h_b^2(1-\lambda) - \rho_b g h_b^2(1-\lambda)\frac{1-sin\phi}{1+sin\phi} + 2C\sqrt{\frac{1-sin\phi}{1+sin\phi}} \tag{9}$$

The force required for extensional failure is then derived by integrating S_F over the thickness h_b (Schueller and Davy, 2008):

$$F_F = \int\limits_{h_b} S_F dz = \frac{1}{2}\rho_b g h_b^2(1-\lambda) - \frac{1}{2}\rho_b g h_b^2(1-\lambda)\frac{1-sin\phi}{1+sin\phi} + 2Ch_b\sqrt{\frac{1-sin\phi}{1+sin\phi}} \tag{10}$$

The viscous behavior of a salt layer is characterized by a stress-strain rate relationship. Rock salt (halite), which usually constitutes the main volumetric proportion of a mobilized evaporitic succession (Jackson and Hudec, 2017), deforms by a combination of dislocation and diffusion (solution-precipitation) creep mechanisms depending on grain size, temperature, strain rate, percentage of intercrystalline fluids and confining pressure (e.g. Schléder et al., 2008; Urai et al., 2008). The large-scale deformation behavior is suggested to be an average of these creep laws (Weijermars and Schmeling, 1986). At relatively low strain rates (<$\sim 10^{-13}$ s^{-1}), low confining pressure (<10^6 Pa), grain sizes of <1 cm and typical temperature range (20–200°C), rock salt deformation is dominated by diffusion creep, which is characterized by a linear stress-strain rate relationship (Newtonian fluid) (Van Keken et al., 1993). At higher strain rates and confining pressure, the deformation is a combination of diffusion and dislocation creep so that the shear stress-strain strain rate relationship is logarithmic (power-law fluid) and salt shows a strain rate softening behavior (Urai et al., 2008; Van Keken et al., 1993). Silicone putty, which is commonly used in salt tectonic experiments, possesses a strain rate softening behavior for strain rates >10^{-2} s^{-1} (Rudolf et al., 2016). However, such high strain rates are not reached in the presented models. Thus, for modeling purposes, the salt layer is here approximated as temperature-independent, mechanically uniform ductile material with a linear (Newtonian) stress-strain rate behavior. This condition might be true for wet salt (>$\sim$0.05 wt% water content) with relatively small grain sizes (<0.5 mm) (Urai et al., 2008). Under this assumption, differential (viscous) stress is calculated by (Weijermars et al., 1993; Bonini et al., 2012; Turcotte and Schubert, 2014):

$$S_V = \sigma_1 - \sigma_3 = \eta\dot{\gamma} \tag{11}$$

Here, η is the dynamic viscosity and $\dot{\gamma}$ the shear strain rate in x-direction, which can be approximated by the shear velocity u_x at the base of ductile layer and the thickness of the viscous layer h_d. Tectonic extension induces a Couette shear flow (Turcotte and Schubert, 2014) at the base of the silicone on the flanks. Integrating Eq. (11) over the thickness of the ductile layer h_d gives the viscous forces:

$$F_V = \int\limits_{h_d} S_V dz = \eta\dot{\gamma}h_d = \eta u_x \tag{12}$$

For comparison between nature and model, we inserted a range of natural and experimental values (Tab. 2) in Eq. (10) and (12) and calculated BDC (Eq. (2)). To achieve correct dynamical scaling, BDC should be equal for model and nature. However, natural values of viscosity (10^{16} – 10^{19} Pas; Van Keken et al. (1993); Mukherjee et al. (2010)) and strain rates (10^{-16} – 10^{-14}s^{-1}; Jackson and Hudec (2017)) can be highly variably so that F_V can vary over several orders of magnitude (Tab.

2). Nevertheless, the curves in Fig. 4a show that BDC for model and nature are relatively similar for a wide range of values, especially for intermediate values.

Equation (10) reveals that the thickness of the overburden h_b mainly governs the coupling between brittle and ductile layer due to its quadratic input. Frictional forces are 1–2 orders of magnitude higher than viscous forces, at least at the beginning of the experiment when strain in the viscous layer is distributed widely. During progressive strain localization in later stage of the experiment, higher strain rates and, hence, higher viscous forces arise. Therefore, the BDC can be a measure for strain localization (Sornette et al., 1993; Schueller and Davy, 2008) in future advanced experiments when strain evolution is quantified.

The ratio between brittle and ductile material properties sets the velocity scaling (extension rate, tilting rate, sedimentation rate) by relating viscosity of the ductile layer, strain rates and characteristic lengths, e.g. the thickness h_b, between model and nature (Weijermars et al., 1993; Allen and Beaumont, 2012):

$$\frac{u_m}{u_n} = \frac{\left(\frac{\rho_b g h_b^2}{\eta}\right)_m}{\left(\frac{\rho_b g h_b^2}{\eta}\right)_n} \tag{13}$$

Applying average values of viscosity, thickness and density (Tab. 2), the velocity scaling ratio is $\sim 10^4$. Natural extension rate can vary between 0.1 and 10 mm a^{-1} so that experimental extension rate should be in the range of $\sim$0.1 to 10 mm h^{-1}. We choose intermediate rates 1 mmh^{-1} for practical reasons so that a simulation duration of several hours to a few days is achieved.

Tectonic stresses and gravity are the main driving factors in the geological scenarios modeled here. For scaling purposes we adapted the 'Argand number' (Ar) from lithospheric scale models of lithospheric brittle-ductile systems (e.g. England and McKenzie, 1982; Schueller and Davy, 2008), which relates tectonic forces to the buoyancy force F_B. The tectonic force is approximated by the integrated strength of the brittle and the ductile layer and, therefore, the sum of F_F (Eq. (10)) and F_V (Eq. (12)). Thus, the Argand number is calculated by:

$$Ar = \frac{F_B}{F_F + F_V} \tag{14}$$

The buoyancy force F_B result from isostatic sinking of the overburden into the ductile substratum, which is calculated by the weight of the overburden depending on thickness and density and the weight of the equivalent volume of the viscous substratum (e.g. Zoback and Mooney, 2003; Schueller and Davy, 2008):

$$F_B = \int\limits_{\Delta h_d} \rho_d g z dz - \int\limits_{h_b} \rho_b g z dz \tag{15}$$

where Δh_d is the amount of subsidence of the overburden into the ductile layer. Under isostatic conditions, Δh_d is:

$$\Delta h_d = \frac{\rho_b h_b}{\rho_d} \tag{16}$$

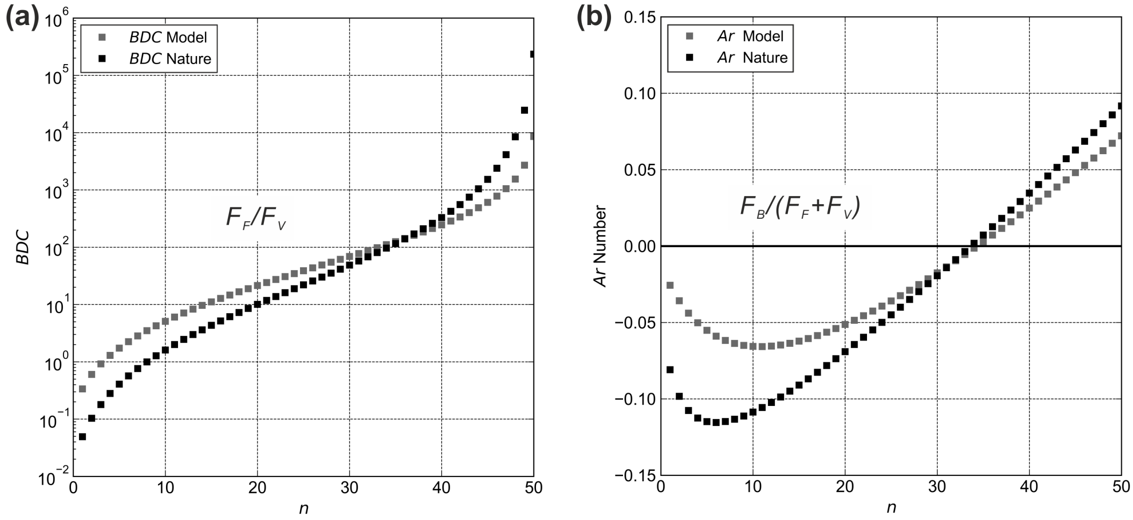

Figure 4. Diagrams of the (**a**) brittle-ductile-coupling (BDC) and (**b**) the Argand number (Ar) for natural and experimental values. To calculate the values for both parameter, a range of n (= 50) different values of the input parameters (Tab. 2, see supplementary material) were inserted in Eq. (2) and 14. Ar - Argand number, BDC – Brittle-ductile coupling, F_B – Buoyancy force, F_F – Frictional force in the brittle layer, F_V – Viscous force in the ductile layer.

After integration, Eq. (15) becomes:

$$F_B = \frac{1}{2} g \rho_b h_b^2 (\frac{\rho_b}{\rho_d} - 1) \qquad (17)$$

The gravitational buoyancy force is mainly influenced by the ratio between overburden and salt density. Salt density is constant with depth, whereas the density of other sediments increases with depth due to compaction. During early stage of the basin history, the overburden density ρ_b is smaller than the salt density ρ_b so that F_B is negative. It changes to positive values when ρ_b exceeds ρ_d. Thus, Ar also changes from negative to positive when inserting a range of potential values (Tab. 2) into Eq. (14) (Fig. 4b). The diagram in Fig. 4b shows that the curve shapes of Ar are similar between model and nature meaning the general behavior of the influence of buoyancy force, which changes the dynamics of flow in the viscous layer, is adequately approximated in the models.

3.4 Density stratification

Whereas the average density of a salt layer is assumed to be nearly constant with depth ($\sim$2150 kg m^{-}3), other sedimentary rocks consolidate during burial (Fig. 5a and b). Due to chemical mineralization and mechanical compaction the porosity ϕ of

Table 2. List of parameters and values used for the scaling procedure, i.e. to calculate BDC (Eq. (2)) and Ar (Eq. (14)).

Parameter	**Sign**	**Dimension**	**Model**	**Nature**	**Scaling factor**
Thickness (brittle layer)	h_b	[m]	0.001–0.03	100–3000	10^{-5}
Thickness (ductile layer)	h_d	[m]	0.005–0.03	500–3000	10^{-5}
Extension rate	u_x	$[\mathrm{mm\,h^{-1}}]$ / $[\mathrm{mm\,a^{-1}}]$	0.1–10	0.1–10	$\sim 10^4$
Strain rate	$\dot{\varepsilon}$	$[\mathrm{s^{-1}}]$	10^{-6}–10^{-4}	10^{-16}–10^{-13}	10^{-6}–10^{-10}
Density (brittle layer)	ρ_b	$[\mathrm{kg\,m^{-3}}]$	800–1050	1850–2300	$\sim$0.45
Density (ductile layer)	ρ_d	$[\mathrm{kg\,m^{-3}}]$	970	2150	$\sim$0.45
Coefficient of internal peak friction	μ	–	0.55–0.65	0.5–0.8	$\sim$1
Cohesion	C	[Pa]	20–60	1–10$\times 10^6$	0.5×10^{-6} –2×10^{-5}
Dynamic viscosity	η	[Pa s]	2.2×10^4–2.8×10^4	10^{17}–10^{19}	10^{-13}–10^{-15}
Lithostatic pressure	σ_L	[Pa]	10–300	5–40$\times 10^6$	$\sim 7 \times 10^{-6}$
Brittle strength	S_F	[Pa]	30–300	2–40$\times 10^6$	0.7×10^{-5}–1.5×10^{-5}
Ductile strength	S_V	[Pa]	0.006–0.08	30–30000	2×10^{-6}–2×10^{-4}
Frictional force	F_F	$[\mathrm{N\,m^{-1}}]$	0.03–5	10^8–10^{11}	7×10^{-11}–16×10^{-11}
Viscous force	F_V	$[\mathrm{N\,m^{-1}}]$	10^{-4}–10^{-2}	10^5–10^9	10^{-9}–10^{-11}
Buoyancy force	F_B	$[\mathrm{N\,m^{-1}}]$	-10^{-3}–10^{-1}	-10^7–10^{10}	$\sim 5\times 10^{-11}$
Brittle-ductile coupling	BDC	–	10^{-1}–10^3	10^{-2}–10^5	0.04–7
Argand number	Ar	–	-0.03–0.07	-0.08–0.09	0.3–1.5

these sediments decreases with depth leading to an increasing density. The most common porosity-depth-relationship is given by Athy's law (Athy, 1930):

$$\phi = \phi_0 e^{-cz} \tag{18}$$

where ϕ_0 and c stand for the initial porosity and the depth coefficient. The corresponding density $\rho_b(z)$ at each depth can then be calculated by using the grain density ρ_G (Fig. 5b) and the density of the pore fluid ρ_f:

$$\rho_b(z) = \phi\rho_f + (1-\phi)\rho_G \tag{19}$$

Integrating over the entire thickness of the cover h_b gives the average density $\overline{\rho_b}$ of the cover:

$$\overline{\rho_b} = \rho_G + \frac{(\rho_G - \rho_f)\phi_0}{c}\frac{(e^{-ch_b} - 1)}{h_b} \tag{20}$$

Because of this density increase, the bulk density of overburden sediments $\overline{\rho_b}$ is smaller than that of salt at shallow depths and exceeds the average salt density at a depth between 2200 and 3800 m (e.g. Jackson and Talbot, 1986; Hudec et al., 2009)

(Fig. 5b). Exceeding this thickness, the overburden is able to autonomously subside into the salt layer and squeeze the salt upwards (Warsitzka et al., 2018).

Compaction of natural sediments cannot be directly simulated in analog models using the common granular materials. However, it is not the density increase itself, but the increase of the lithostatic pressure at the base of the overburden that is the crucial parameter determining differential loading and the pressure gradient in the ductile layer. In order to simulate an appropriately scaled increase of the lithostatic pressure, we increased the density of the sand mixture (ρ_{bmi}) during each step of syn-kinematic sand accumulation, similar to the approach by Dooley and Hudec (2020). This results in an inverse density stratification with less dense material at the bottom and denser material at the top of the cover (Fig. 5c) and a stepwise increase of the bulk density of the entire sand cover. To compare natural with experimental density-depth curves, the standardized density ρ' was calculated by dividing all density values through the density of the salt or the silicone, respectively. Likewise, the depth was standardized by dividing the depth through the maximal thickness of the cover (here: 5 cm in the model and 5 km in nature). The increase in density of each new sand layer has to be set in such a manner that the standardized bulk density resembles the exponential increase of the standardized bulk density in nature (Fig. 5d).

3.5 Experimental procedure

Since all parts of the apparatus can be controlled separately, different modes of basin evolution can be tested, such as pure extension without tilting, pure uplift of the flanks without extension and combined motion of graben and flanks. In the experiment with combined modes (Exp. 3, 6 and 7), extension and tilting was applied simultaneously. This procedure refers to the geological condition that in most rift basins salt was deposited during or after an initial rifting phase (Tab. 1). It can be assumed that early post-salt history is characterized by thermal sag basin subsidence accompanied by additional post-salt rifting.

In a first series of experiments (T1, E1, ET1), no silicone layer was included in order to present benchmark experiments for the displacement and strain patterns of the basal part and to better illustrate the effects of the viscous layer. In experiment including a silicone layer (T2, E2, ET2, ETS1), the silicone layer was covered by a pre-kinematic layer of granular material prior to onset of deformation. Except for experiment ETS1, no syn-kinematic sand accumulation was applied to demonstrate the deformation patterns resulting only from the specific mode. Only ETS1 involves all relevant processes, which should be investigated with this apparatus (extension, tilting, syn-kinematic sedimentation). In intervals of 5 h, syn-kinematic sand is sieved on the model surface, whereas largest thickness is applied in the graben centre and decreasing thickness on the flanks. This is supposed to mimic aggradational sedimentation pattern as observed in most continental basins.

https://doi.org/10.5194/se-2021-17
Preprint. Discussion started: 25 February 2021

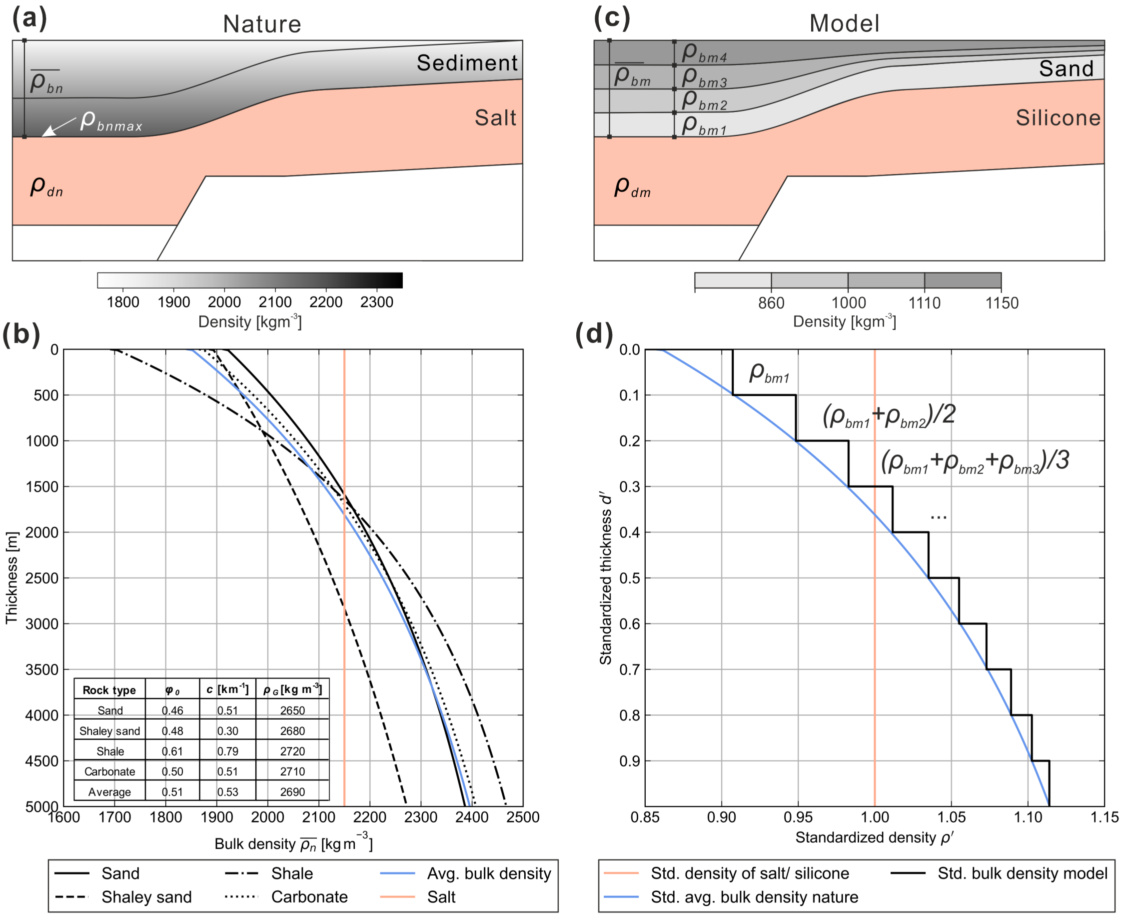

Rock type	φ_0	c [km^{-1}]	ρ_G [kg m^{-3}]
Sand	0.46	0.51	2650
Shaley sand	0.48	0.30	2680
Shale	0.61	0.79	2720
Carbonate	0.50	0.51	2710
Average	0.51	0.53	2690

Figure 5. Density configuration in natural prototype and in the analogue model. (**a**) Natural sediments compact during burial leading to increasing density ρ_{Cn} with depth. (**b**) Curves of the bulk density $\overline{\rho_{Cn}}$ for different sediment types related to the thickness of the overburden. Due to physical compaction accorindg to Athy's law (Athy, 1930), the density increases exponentially with depth. The blue curve shows the bulk density calculated by using average (avg.) values listed in the table. (**c**) Inverse density stratification in the analog models presented here. Layers with increased density are sieved in leading to an increasing bulk density during subsidence. (**d**) Standardized (Std.) thickness and density values for nature and model. Thickness was standardized by the (presumed) maximum thickness of the overburden (nature: 5 km/model: 5 cm). Density values were standardized by dividing the density of the cover (nature: ρ_{Cn}/ model: ρ_{Cm}) by the density of the viscous layer (nature: $\overline{\rho_{Sa}}$/ model: $\overline{\rho_{Si}}$). Note that the density of each sieved layer in the models increases upwards. This procedure is applied to increase the bulk density of the subsiding overburden in a similar manner as in nature. phi_0 – initial porosity, c – depth coefficient, ρ_G – grain density.

Table 3. Experiments and key parameters. d_e – total amount of vertical displacement of the graben centre, d_t – total amount of vertical uplift of the graben flanks, h_b the thickness of the pre-kinematic sand layer, h_d – thickness of the silicone, T – total duration of the experiment, u_e – extension rate, u_e – uplift rate of the flanks.

Experiment No.	Experiment Name	h_b [cm]	h_d [cm]	u_e [mm h^{-1}]	d_e [mm]	u_t [mm h^{-1}]	d_t [mm]	T [h]	Comment
1	E1	0.3	0.0	1	20	0	0	20	No silicone
2	E2	0.3	1.5	1	20	0	0	20	–
3	T1	0.3	0.0	0	0	1	20	20	No silicone
4	T2	0.3	1.5	0	0	1	20	20	–
5	ET1	0.3	0.0	1	20	1	20	20	No silicone
6	ET2	0.3	1.5	1	20	1	20	20	–
7	ETS1	0.3	1.5	1	20	1	20	20	Including syn-kinematic sedimentation

4 Results

4.1 With vs- without viscous substratum

A first series of experiments (E1, T1, ET1) was conducted without a viscous silicone layer to illustrate the movement of the basal parts and to compare them to displacement patterns developed in experiments containing a viscous substratum (E2, T2, ET2).

When only lateral extension was applied as boundary condition (experiment E1), both flanks were pushed laterally by the downward moving central graben block (Fig. 6a). In experiment E2, this outward directed movement was overprinted by deformation of the cover layer and the viscous substratum close to the central graben (Fig. 6b). The cover layer moved inward (max. 70 mm in 20 h) indicating an influx of silicone into the graben. Figure 6c and d display the evolution of x-displacement d_x extracted from a profile through the centre of the box. It shows that the inward movement in E2 began during the late stages of the syn-extensional phase and continued after extension stopped (post-extensional phase).

Figure 6e and f display the averaged cumulative x-displacement d_{Xcum} separately for the left (blue) and the right (green) half of the box. In both experiments, E1 and E2, d_{Xcum} increased linearly with progressive lateral extension. However, towards the end of the extensional phase of exp. E2, d_{Xcum} was increased. This reflects the effect of the movement of the cover towards the graben structure and implies that this movement was faster than the lateral extension.

In experiment T1 (without silicone) in which only tilting of the flanks was applied, minor x-displacement above the flanks can be observed (Fig. 7a and c). In the experiment T2 (including a viscous layer), the tilting of the flanks caused a widespread movement of the cover layer towards the centre of the box (max. 3 mm in 20 h) indicating a downward redistribution of the silicone (Fig. 7b). The evolutionary plot in Fig. 7d shows that this downward movement began after a relatively small amount of tilting (5 h; ∼5 mm flank uplift). The downward movement only continued after tilting stopped, for a short extent (∼2 h; Fig. 7f).

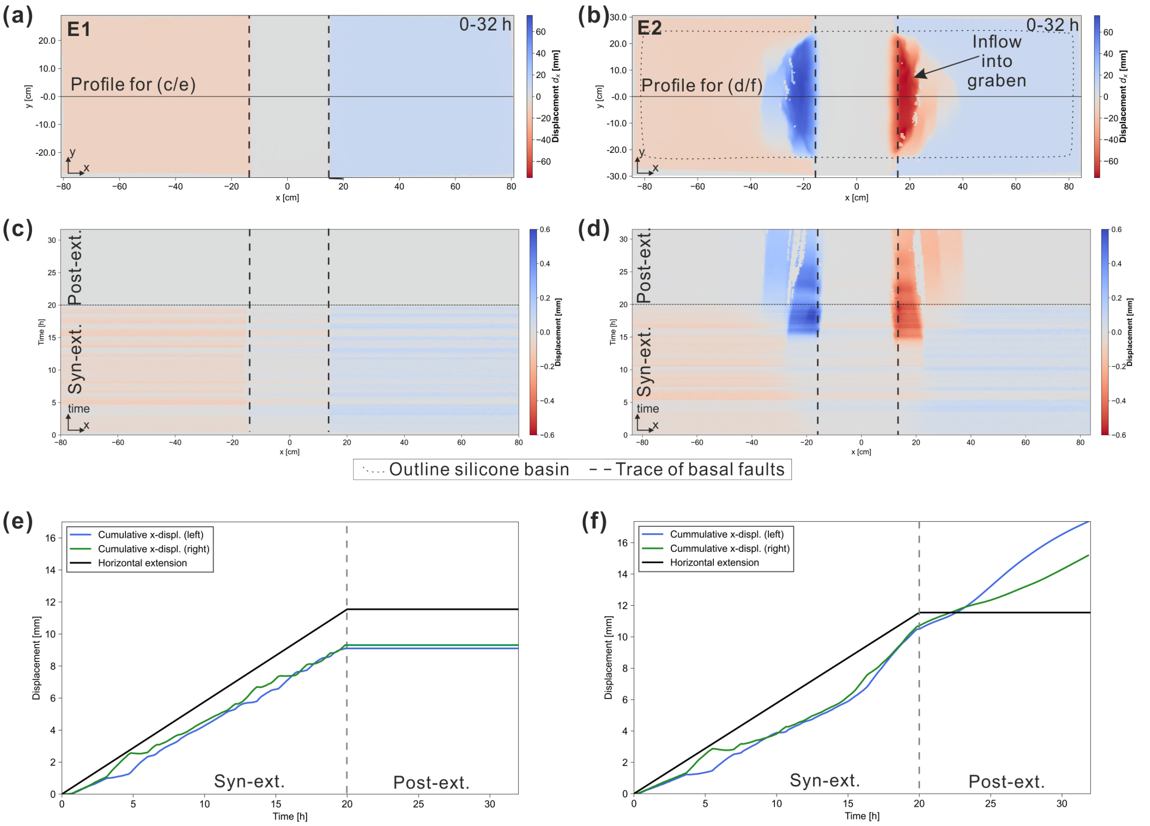

Figure 6. Results of the DIC of experiment E1 (without viscous substratum) and E2 (with viscous substratum) in which only lateral extension with a rate of 1 mm h^{-1} was applied. The total vertical displacement of the central block is 2 cm. **(a/b)** Top view of the cumulative x-displacement (d_x) at the end of the experiment (32 h). Blue colors reflect rightward and red colors leftward movement. **(c/d)** Incremental x-displacement extracted from a central profile and plotted against experimental time. **(e/f)** Averaged cumulative x-displacement for the left (blue) and the right (green) half of the box plotted against experimental time. Note that the black line displays the lateral extension (max. ∼12 mm), which is less than the vertical movement of the central block (max. 20 mm).

In experiments ET1 and ET2, graben extension and flank tilting were applied as boundary conditions (Fig. 8). With the presence of a viscous layer, the inward movement of the cover layer towards the subsiding graben affected the entire region of the uplifted flanks (Fig. 8b). Inward movement was at a maximum close to the basal normal faults (∼100 mm in 20 h) and
295 reflects the downslope gliding of the cover and silicone. The evolutionary map shows that the downslope movement appears to be activated at roughly half of the syn-extensional phase (∼1 cm of subsidence of the graben and ∼1 cm uplift of the flanks) (Fig. 8d). During the post-extensional phase, downslope gliding continued. The averaged cumulative x-displacement d_{Xcum} increased strongly towards the end of the syn-extensional phase and still increased linearly during the post-extensional phase (Fig. 8f), which implies that the downward movement of the cover layer continued at a relatively high velocity.

https://doi.org/10.5194/se-2021-17
Preprint. Discussion started: 25 February 2021

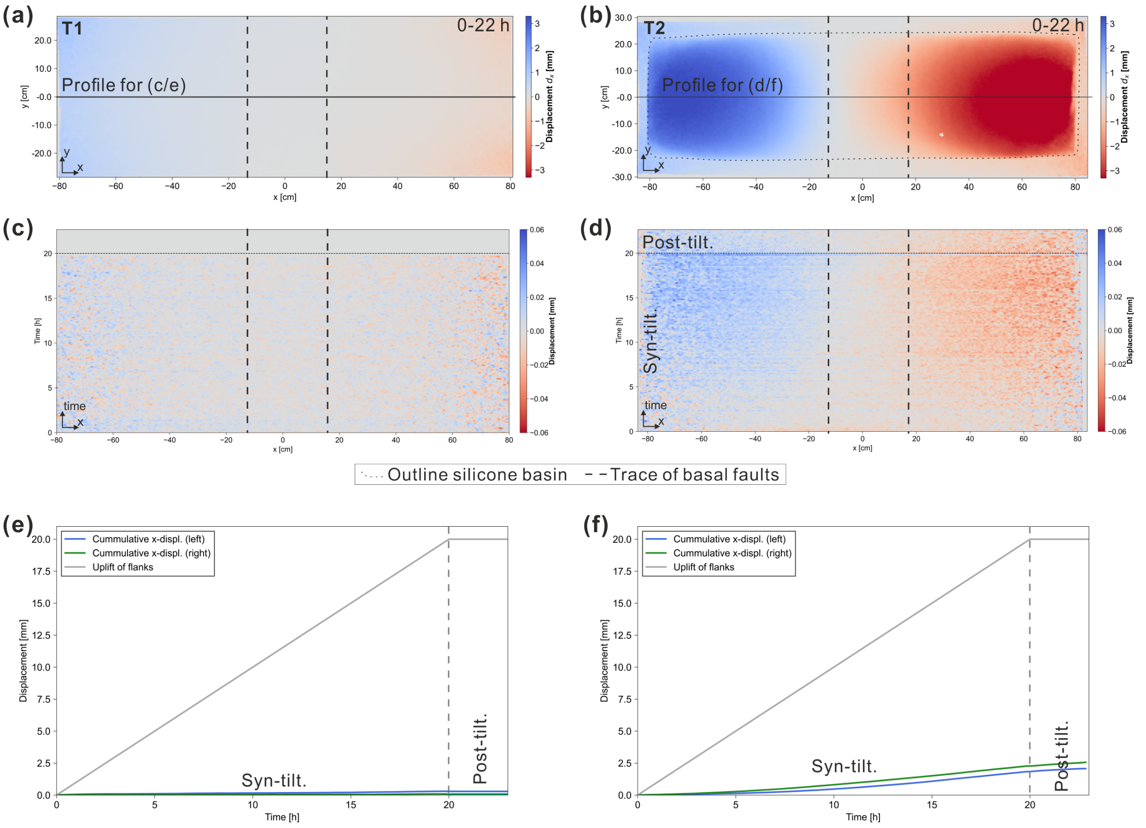

Figure 7. Results of the DIC of experiment T1 (without viscous substratum) and T2 (with viscous substratum) in which tilting was applied with a rate of 1 mm h^{-1}. The total vertical displacement of the flanking plates is 2 cm. (**a/b**) Top view of the cumulative x-displacement (d_x) at the end of the experiment (23 h). Blue colors reflect rightward and red colors leftward movement. (**c/d**) Incremental x-displacement extracted from a central profile and plotted against experimental time. (**e/f**) Averaged cumulative x-displacement for the left (blue) and the right (green) half of the box. The gray line presents the uplift of the flanks, which was equal for both sides.

4.2 Flat vs. tilting flanks

The effects of inclined flanks (Fig. 9a and b) on the structural development is evaluated by comparing experiments E2 and ET2. Figure 9c and d show that the total amounts of x-displacement d_x were significantly higher and deformation affects a larger region, if the flanks were tilted contemporaneously with the basal extension. Especially during the post-extensional phase, widespread downward movement can be observed in the entire silicone basin in ET2, whereas deformation is still limited to regions close to the basal graben in E2 (Fig. 9e and f). In both experiments, the region affected by downward movement adjacent to the graben becomes wider after extension stopped. Furthermore, the total amount of d_x and, therefore, the displacement rates are considerably higher in the post-extensional phase (12 h) than in the syn-extensional phase (20 h).

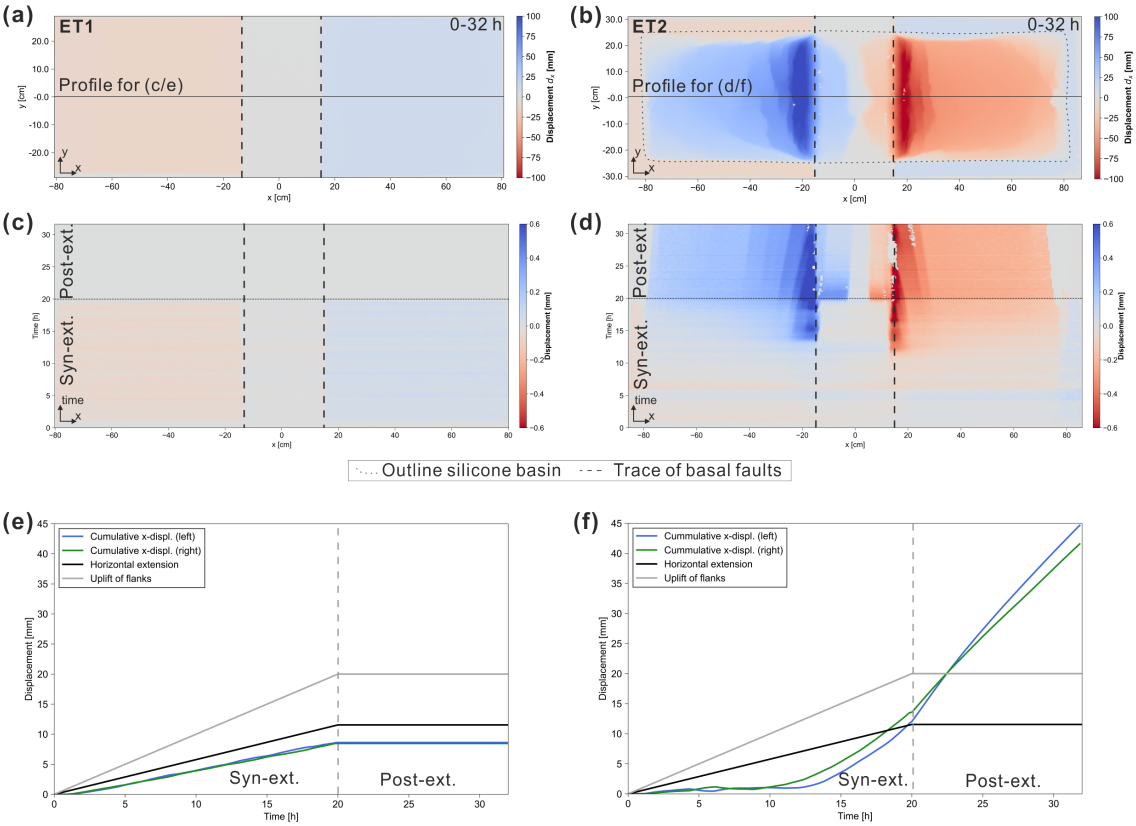

Figure 8. Results of the DIC of experiment ET1 (without viscous substratum) and ET2 (with viscous substratum). In both experiments extension and titling with rates of 1 mm h^{-1} were applied. The total vertical displacement of the central block and the flanking plates is 2 cm. **(a/b)** Top view of the cumulative x-displacement (d_x) at the end of the experiment (32 h). Blue colors reflect rightward and red colors leftward movement. **(c/d)** Incremental x-displacement extracted from a central profile and plotted against experimental time. **(e/f)** Averaged cumulative x-displacement for the left (blue) and the right (green) half of the box.

The evolutionary maps (Fig. 9g and h) demonstrate that the onset of inward movement into the central graben began towards the end of the syn-extensional phase in both experiments and did not occur noticeably earlier in ET2.

The patterns of the normal strain in x-direction e_{xx} (Fig. 10a) reveal that extensional fault zones developed at an offset of roughly 10 cm from the basal faults ('graben-edge extension') in E2, whereas compressional strain occurred directly above the basal faults. The extensional fault zones propagated away from the graben during the post-extensional phase (Fig. 10b). In ET2, graben-edge fault zones were located closer to the graben (<8 cm). Additional extensional fault zones occurred at the outer margins of the silicone basin ('basin-margin extension') (Fig. 10a). During the post-extensional phase, the graben-edge extension propagated upslope, whereas the basin-margin extension migrated downward. Compressional zones evolved in the centre of the subsided graben, which reflects the influx of the silicone and downslope gliding of the sand cover into the graben. In contrast, compressional strain in E2 was limited to the regions close to the basal faults. The main difference between

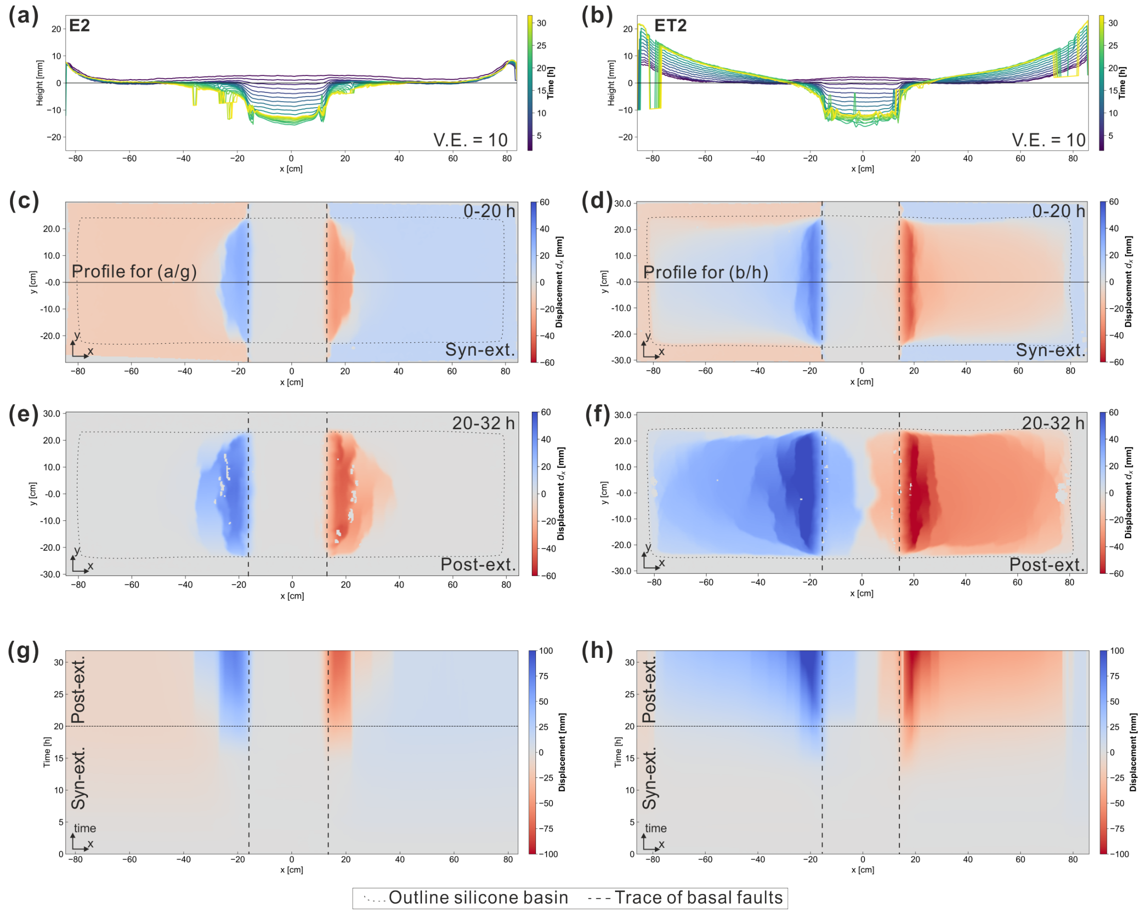

Figure 9. Comparison of displacement patterns between experiment E2 (left) and ET2 (right). (**a/b**) Evolution of the surface elevation extracted along a center line. (**c/d**) Cumulative x-displacement d_x at the end of the syn-extensional phase. (**e/f**) Cumulative x-displacement d_x at the end of the post-extensional phase. (**g/h**) Evolutionary maps showing the cumulative x-displacement plotted against the experimental time. Blue means rightward and red leftward movement.

experiment E2 and ET2 is that the amount of the extensional strain at the graben-edge fault zones was higher in E2 ($\sim$2) than in ET2 ($\sim$1.5) and graben-edge extension was distributed over a wider region in the E2 (Fig. 11). It also can be observed that extended and dissected cover blocks are convexly curved in E2, whereas they strike roughly parallel to the basal faults in ET2 (Fig. 11a and c).

4.3 Effects of syn-kinematic sedimentation

In ETS1 extension and tilting of the basal parts was accompanied by regular intervals of syn-kinematic sand accumulation. Similar to ET2, a downslope gliding of the overburden above the flanks can be observed (Fig. 12a). However, the total amount of x-displacement at the end of the extensional phase is smaller in ETS1 (max. 10 mm) than in ET2 ($\sim$40 mm). The difference is

https://doi.org/10.5194/se-2021-17
Preprint. Discussion started: 25 February 2021

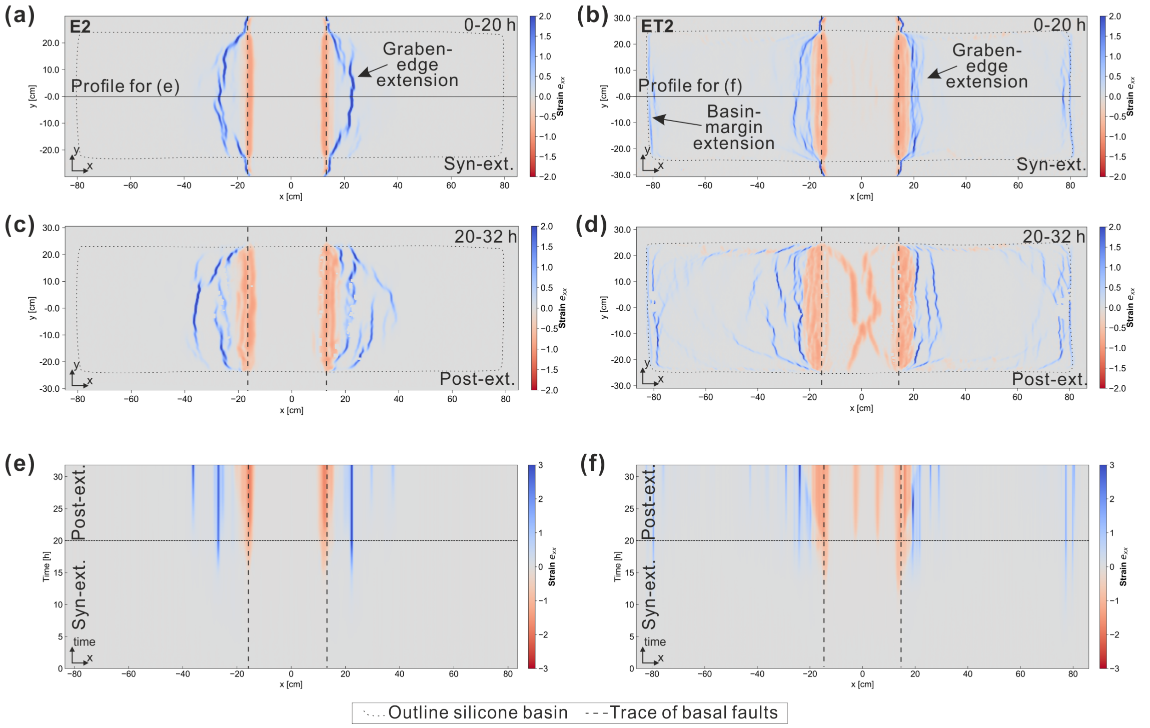

Figure 10. Comparison of strain patterns between E2 (left) and ET2 (right). (**a/b**) Cumulative normal strain in x-direction e_{xx} at the end of the extensional phase. (**c/d**) Cumulative e_{xx} at the end of the post-extensional phase. (**e/f**) Evolutionary maps showing the cumulative e_{xx} plotted against the experimental time. Blue means extensional and red compressional strain.

even higher for the total d_x at the end of the post-extensional phase (ETS1: 1.5 mm; ET2: 60 mm). This implies that sequentially filling of the downslope depocentre with syn-kinematic sand significantly reduces downslope gliding of the cover. Graben-edge extension and compressional strain in the graben centre were almost completely suppressed in ETS1 (Fig. 12b). The total amount of strain at the basin-margin extensional fault zones (Fig. 12b and d) was also less than in ET2 (Fig. 10b and d). Strain is focused on a 1–2 discrete zones in ETS1 and, hence, is more localized compared to the widely distributed strain observed in ET2.

During the post-extensional phase, downslope gliding was restricted to the regions of the graben flanks (Fig. 12a). Diffuse, widespread compressional strain occurred in the central parts of the flanks (Fig. 12b) and not above the graben centre as in ET2 (Fig. 10d). The evolutionary plots in Fig. 12c and d show that incremental displacement and strain reached their maximum at the end of the extensional phase and only slowly continued after extension and tilting was stopped. This is also in contrast to ET2, where maximum amounts of displacement and strain were achieved during the post-extensional downslope gliding.

Cross sections cut through the final experiment reveal that the structures of basin-margin extensional fault zones are characterized by synthetic rollovers and symmetric grabens (Fig. 13a and b). Strongest deformation occurred directly at the pinch

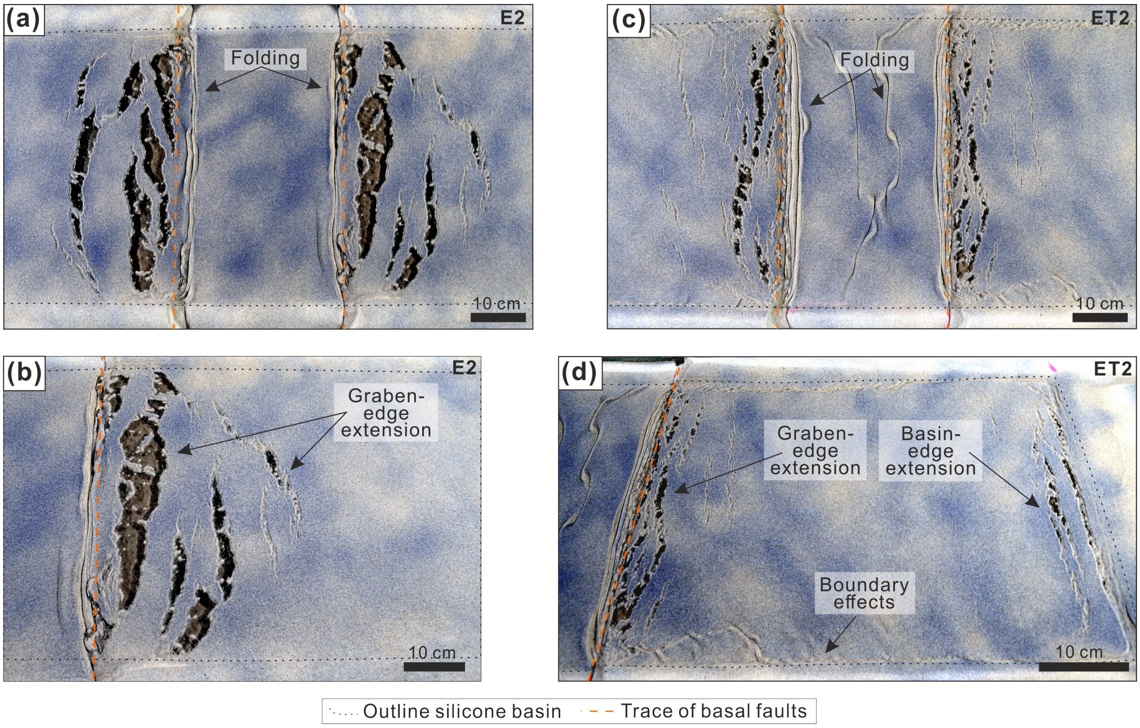

Figure 11. Photos of the final stage of the experiments (end of the post-extensional phase) of E2 and ET2. (**a**) Top-view photo of the graben-edge extension and exposed silicone in E2. Compressional folds occur close to the hanging wall edges of the basal faults. (**b**) Perspective view of the right flank of E2. (**c**) Top view photos displaying the graben-edge extension above the graben flanks and the folding in the centre of the graben in ET2. (**d**) The perspective view of the right flank of ET2 including the graben-edge and basin-margin extensional zones.

out of the silicone layer. Aside from minor extensional thinning of the pre-kinematic layer, no deformation structures can be observed close to the basal faults (Fig. 13c).

5 Discussion

5.1 Experimental procedure

The presented experiments on gravity-driven deformation in salt-bearing rift basins (SBRB) provide first insights into the influence of flank tilting on basin-wide deformation patterns. The comparison between experiments with and without tilting of the flanks illustrate how local deformation structures due to a sub-salt graben are affected by regional-scale flow of the viscous material. When graben flanks remain flat, deformation is restricted to areas in the vicinity of the basal graben even though thin-skinned extensional zones are decoupled from the basal normal faults (Fig. 10a). Due to tilting of the flanks in experiment ET2, lateral displacement of the brittle overburden is induced over the entire area underlain by a viscous layer. Total amounts of syn- and post-extensional displacement were considerably larger compared to those in the experiment without tilting (E2).

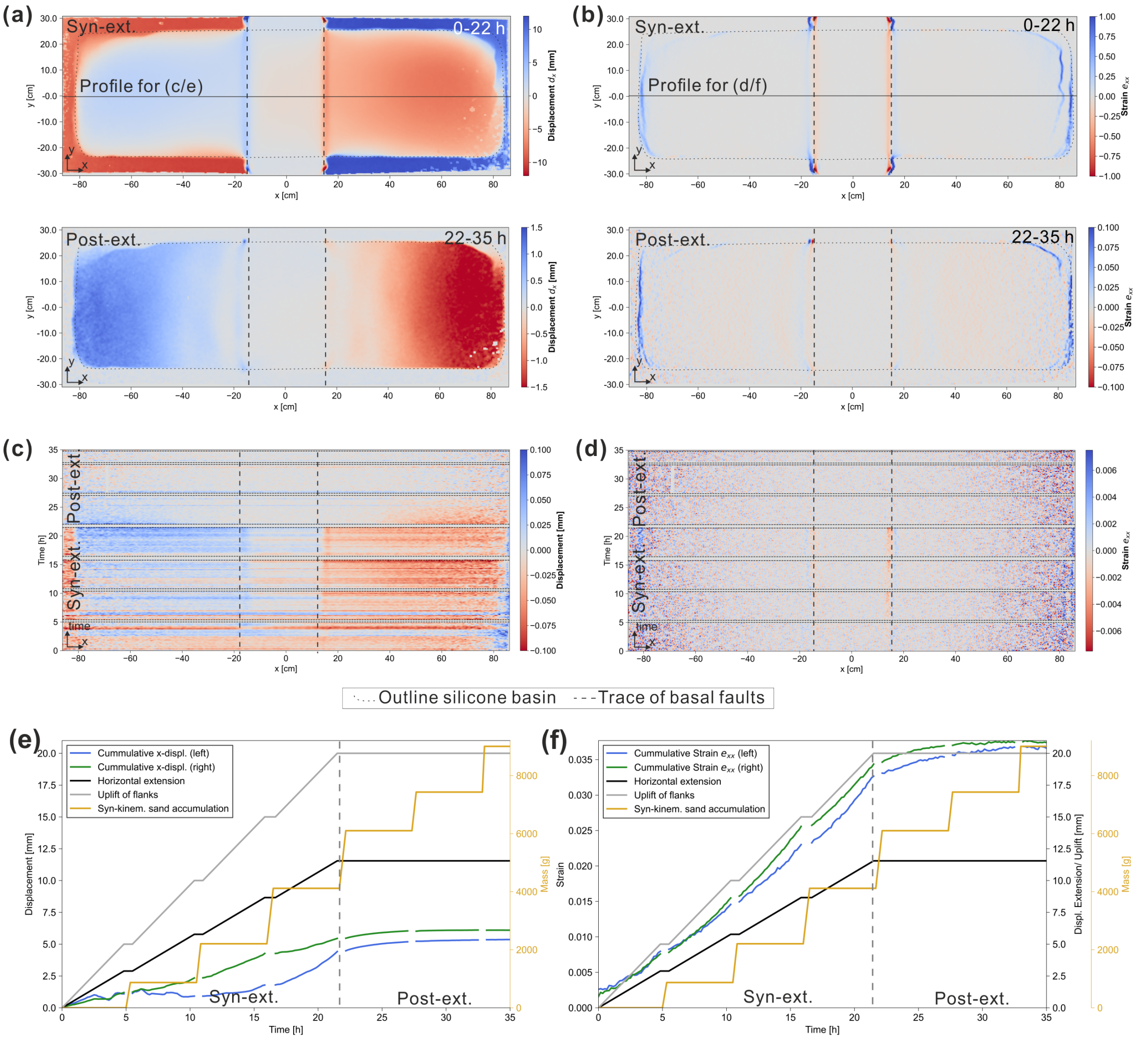

Figure 12. Displacement and strain patterns experiment ETS1 (extension + tilting + sedimentation). (**a**) Cumulative x-displacement (d_x) and (**b**) cumulative x-normal strain (e_{xx}) at the end of the syn-extensional (20 h) and post-extensional phase (32 h). (**c**) Evolutionary map showing the incremental d_x and (**d**) the incremental e_{xx} plotted against the experimental time. (**e**) Averaged cumulative d_x and (**f**) averaged cumulative e_{xx} for the left (blue) and the right (green) half of the box.

Nevertheless, extensional strain in the graben-edge fault zones is less in ET2 than in E2 (Fig. 10a and b). These observations indicate that the amount of graben-edge extension is decreased by downslope gliding of the cover layer. In terms of kinematic balancing and cross section restoration, this implies that there is a deficit in the balance between sub- and supra-salt extension close to the graben centre.

During the post-extensional phase, downslope gliding continues across the entire graben flanks in ET2, which enhanced extension at the basin margin and caused shortening of graben-edge extensional fault zones as well as fold and thrust faults in

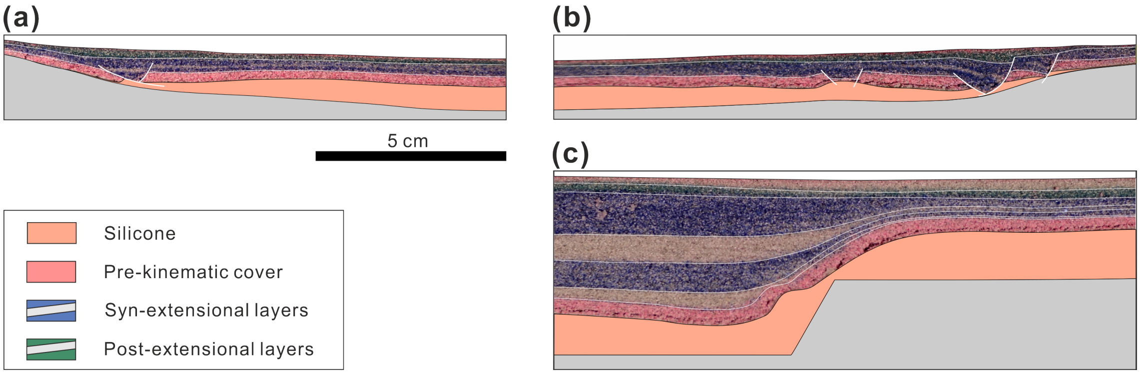

Figure 13. Cross sections cut through the centre of Exp. ETS1 in which syn-kinematic sand accumulation was applied during and after basal extension. (**a**) Cross section of the extensional fault zone at the left basin margin. (**b**) Cross section of the extensional fault zone at the right basin margin. (**c**) Cross section of the syn-kinematic strata close to the right basal fault. Structures above the left basal fault were similar.

the the graben centre. We suggest that basin-margin fault zones and shortened graben fault zones, in particular if they are active subsequent to the rifting, are diagnostic indicators for the influence of gravity gliding on the structural dynamics in natural rift basins.

The experiment with syn-kinematic sedimentation (ETS1) demonstrates that the ability of downward gliding is reduced by sediment accumulation in the basin centre. In particular during the post-extensional phase, gravity driven deformation decreased rapidly after the first post-extensional step of sand accumulation. This suggests that gravity gliding is not a compelling processes in SBRB with tilted flanks and might depend on the amount and accumulation rate of sediments in the basin centre. Experiment ET2 (without sedimentation) and ETS1 (including sedimentation) might represent end-member types of SBRB of an underfilled basin (low sedimentation rates) and overfilled basin (high sedimentation rates). Gravity gliding is favored in underfilled rift basins or basin experiencing fast flank uplift, respectively. High sediment accumulation rate, in contrast, might effectively prevent gravity gliding. However, such a conclusion require a more comprehensive parameter study in which various ratios of sedimentation vs. tilting rates are tested.

5.2 Limitations of the apparatus and the procedure

In our experimental setup, basal extension is focused on two parallel faults, which is a simplification of a natural rift basin. Natural rift basins and the process of crustal extension include greater complexities than presented in our experimental setup. Rift basins usually consist of overlapping fault systems with normal faults, fault intersection, ramps, strike-slip segments and intrabasinal ridges. Such diverse fault patterns in the sub-salt basement determines the distribution of the original salt, its post-depositional redistribution and localization of salt structures (e.g. Koyi et al., 1993; Dooley et al., 2005; Dooley and Hudec, 2020). Similarly, the flanks in our model setup have an even base, whereas in nature small offset faults occur in these regions due to, for instance, widening of the graben through time. Basal discontinuities influence the strain localization in the viscous and brittle layers mainly because of abrupt changes of the thickness of the ductile layer (Dooley et al., 2017) so that basin-margin extension zones are distributed above such basal steps rather then at the marginal pinch-out of the viscous layer.

Natural rift basins often possess asymmetrical half graben shapes characterized by a large-offset normal fault on one side and a smoothly tilted, slightly faulted flank on the other. In such half grabens, decoupled extension, probably caused by gravity gliding, can occur above the slightly tilted flank (e.g. Coward and Stewart, 1995; Thomas and Coward, 1996; Ge et al., 2017; Jackson and Hudec, 2017). Such alternative basin shapes cannot be modeled here, but should be considered and discussed when interpreting the modeling results. Our experimental approach is to initially simplify the geometrical boundary conditions, and in later experimental studies, further complexities can then be introduced, such as static structural discontinuities can be inserted in the sub-silicone base to examine lateral variation of the strain patterns depending on initial thickness of the viscous layer.

A technical issue can be observed in Fig. 6c and d showing the incremental lateral movement of the flanks. Especially at the beginning of the extensional phase, this movement is not continuous and symmetrical on both sides, which likely results from mechanical locking of the graben block on the basal faults. This effect cannot be avoided even by using lubricants on the faults. Finally, the cumulative displacement of the extensional movement over longer time periods is smooth and regular as observed in Fig. 9c and d.

5.3 Application to nature and outlook

In many SBRB worldwide (Tab. 1), the basin floor at the flanks is inclined and thin-skinned extensional faults occur in the supra-salt cover at the basin margins. The seismic examples shown in Fig. 14 resemble the basin-margin extensional fault zones observed in our experimental cross sections (Fig. 13). Thus, it can be proposed that these natural examples were also formed partly by gravity-driven extension. If so, our experimental results suggest that these natural faults should have been activated in the late stage of the rifting in the main graben and show continued active faulting post-rifting. Such temporal relationships have to be evaluated in detail by cross section balancing for specific rift basins.

The tectonic and sedimentary conditions in the basins of the shown examples were very different. One of the most prominent examples of overlapping gravitationally and tectonically driven supra-salt extension can be found at the western flank of the northern Central Graben (North Sea). Rollover structures and separated overburden blocks ('rafts') developed above the tilted outer platforms of the graben contemporaneously with the Triassic rifting phase of the graben (Fig. 14a) (Hodgson et al., 1992; Buchanan et al., 1996; Penge et al., 1999; Stewart and Clark, 1999). At the North Iberian rifted margin, rollovers detached on pre-rift Triassic evaporites during hyperextension in the Cretaceous (Fig. 14b) (Jammes et al., 2010; Lagabrielle et al., 2010). At the eastern flank of the Red Sea basin basinward listric faults developed on top of the mid-Miocene salt detachment coeval to the development of a fold belt and salt canopies in the basin centre (Fig. 14c) (Heaton et al., 1995). The amount of tectonic stretching and subsidence were relatively large in these three examples – the Iberian margin and the Red Sea Basin translated to early stage passive margins after mobilization of the salt. This probably resulted in steep slopes of the basin floor early on and a basin centre underfilled by sediments. We suggest that these geological conditions promoted intense gravity gliding. Nevertheless, clear evidence for syn-gliding contractional structures are lacking, except for the Red Sea Basin (Heaton et al., 1995).

Extensional fault zones developed above gently dipping flanks of the Polish Basin from Late Triassic to Jurassic, in particular along the NE flank located above the East European Craton (Fig. 14f) (Krzywiec, 2006a, 2012). At the northern edge of the Norwegian-Danish Basin, triangular diapirs of Permian salt and tilted blocks in the overburden are supposed to be triggered by an inclined basin floor during the Triassic (Fig. 14e) (Geil, 1991; Clausen et al., 2015). In these basins, however, reactive diapirs and deeply subsided minibasins evolved in the basin centre coeval to basin-margin extension. Thus, hints for compressive structures due to gravity gliding are difficult to find here as well. Geil (1991) proposed a conceptual model, which stated that loading-driven upward directed salt flow in the basin centre took place contemporaneously to gravity-driven downward salt flow at the inclined graben flanks.

In the Sole Pit Basin, decoupled extensional grabens and listric faults overlie a slightly faulted salt base at the basin margins (Fig. 14f). These extensional structures coincided with the formation of compressive, salt-cored anticlines in the basin centre during the Triassic (e.g. Hughes and Davison, 1993; Coward and Stewart, 1995; Stewart and Coward, 1995). In the Ems Trough (NW-Germany) and the southeastern North Sea, the pre-kinematc overburden (lowermost Lower Triassic) was separated into individual blocks potentially due to raft tectonics (e.g. Thieme and Rockenbauch, 2001; Mohr et al., 2005; Vackiner et al., 2013). Mohr et al. (2005) determined that this coincided with the formation of salt anticlines further downslope. In these examples, upslope extension is partly balanced by downslope compressional structures.

Listric growth faults developed in the post-salt strata on the western flank of the Horn Graben (Southern North Sea) (Fig. 14g) (Best et al., 1983; Baldschuhn et al., 2001). However, the underlying sub-salt base is only slightly inclined and faulted. Thus, it is suggested that supra-salt fault zones are rather detached from sub-salt normal faults in the nearby graben structure and purely tectonically driven (Nalpas and Brun, 1993). This example demonstrates that there are structural similarities between tectonically and gravitationally driven thin-skinned fault zones underlining the necessity to find distinct structural and kinematic characteristics of both drivers.

These examples imply that there are three different scenarios of the interaction between gravity gliding and crustal extension: (1) Gravity gliding took place during strong rifting but no or minor shortening occurred in the basin centre, since here sub-salt faulting created sufficient space to accommodate and hide shortening (probably in the northern Central Graben), (2) Gravity gliding is superimposed with minor rifting and caused basin-margin extension balanced by basin-centre shortening (e.g. in the Sole Pit Basin), and (3) no or only minor gravity gliding occurred, and the thin-skinned extensional structures were mainly tectonically driven (e.g. in the Horn Graben). In order to investigate these scenarios and their governing parameters and processes, a comprehensive analog modeling study has to be performed, modifying variables such as extension rate, tilting rate, layer thickness and timing of tilting in relation to extension.

6 Concluding remarks

Our experimental apparatus successfully reproduced the overlapping influence of tectonic extension and gravity gliding on salt flow and salt structure evolution in salt-bearing rift basins. The apparatus is suitable for simulating crustal extension within a symmetric graben structure and thermal subsidence, which is represented by vertical uplift of the graben flanks. Since basal extension and flank tilting can be controlled separately, the effects of both processes can be investigated separately or combined. Furthermore, we applied mixtures of quartz sand and silicate cenospheres as analog for brittle overburden sediments. This enabled us to vary the ratio between overburden and viscous layer density so that the process of density inversion due to compacting overburden sediments can be produced.

The preliminary experimental study shown here reveals primary structural and kinematic differences depending on the presence of flank tilting. When the graben flanks remain flat during extension, deformation is concentrated in regions close to the basal graben structure. Extensional fault zones develop in the footwall, while overburden above the basal normal faults slides into the graben. When the graben flanks become tilted simultaneously to graben extension, similar deformation patterns occur close to the graben. However, they are overprinted by gravity gliding inducing widespread basin-wide downward movement of the overburden into the central graben. Consequently, additional extension localizes at the upslope basin margins, which is enhanced after basal extension and tilting have stopped. This extension is accommodated in the graben region by reduced amounts of extension on the graben-edge fault zones and compressional strain above the graben bounding faults. If syn-kinematic sedimentation is included in the experimental procedure, lateral downward directed displacement is significantly reduced especially during the post-extensional phase. Furthermore, strain in the margin-edge extensional zones is localized on less, discrete faults.

Observed basin-margin extensional structures in the preliminary experiments resemble typical thin-skinned extensional structures occurring at the flanks of many salt-bearing rift basins with inclined sub-salt bases. Such diagnostic structures indicate that gravity gliding might play an important role in the post-salt structural development.

Data availability. Data of the experiments presented in this study will be provided in a data publication on pangaea.de. The data was submitted and is currently processed (Nr.: PDI-27047).

Code and data availability. No codes are published along with this manuscript

Author contributions. MW invented the concept of this modeling study, designed the experimental apparatus, performed the experiments and composed main parts of the manuscript. Furthermore, data processing and analysis was undertaken by MW. PZ advised the designing and construction of the apparatus and assisted during the experiments. Theoretical input for planing the project, the model design and the concept of the experiments came from FJK. PK supported the comparison of the experiments with the natural case study of the Polish Basin. FJK, PK and PZ helped with finalizing the manuscript.

Competing interests. The authors declare that they have no conflict of interest.

Acknowledgements. The research position of Michael Warsitzka is supported by Czech Academy of Science (AVCR) in frame of the ”Programme to support prospective human resources – post Ph.D. candidates” (Nr.: L100121901). This paper was prepared within a bilateral research project between the Institute of Geophysics of the Czech Academy of Sciences and the Institute of Geological Sciences of the Polish Academy of Sciences (Project nr.: PAN-20-04). We thank Jiří Semerád for helping with designing and for constructing the experimental apparatus.

References

Adam, J., Urai, J. L., Wieneke, B., Oncken, O., Pfeiffer, K., Kukowski, N., Lohrmann, J., Hoth, S., Van der Zee, W., and Schmatz, J.: Shear localisation and strain distribution during tectonic faulting – new insights from granular-flow experiments and high-resolution optical image correlation techniques, J. Struct. Geol., 27, 283–301, https://doi.org/10.1016/j.jsg.2004.08.008, 2005.

Allen, J. and Beaumont, C.: Impact of inconsistent density scaling on physical analogue models of continental margin scale salt tectonics, J. Geophys. Res.: Solid Earth, 117, https://doi.org/10.1029/2012JB009227, 2012.

Alves, T. M., Gawthorpe, R. L., Hunt, D. W., and Monteiro, J. H.: Jurassic tectono-sedimentary evolution of the Northern Lusitanian Basin (offshore Portugal), Mar. Pet. Geol., 19, 727–754, https://doi.org/10.1016/S0264-8172(02)00036-3, 2002.

Athy, L. F.: Density, porosity, and compaction of sedimentary rocks, AAPG Bull., 14, 1–24, https://doi.org/10.1306/3D93289E-16B1-11D7-8645000102C1865D, 1930.

Baldschuhn, R., Binot, F., Fleig, S., Kockel, F., (Hrsg.) unter Mitarbeit von: Best, G., Brückner-Röhling, S., Deneke, E., Frisch, U., Hoffmann, N., Jürgens, U., Krull, P., Röhling, H.-G., Schmitz, J., Sattler-Kosinowski, S., Stancu-Kristoff, G., and Zirngast, M.: Geotektonischer Atlas von Nordwest-Deutschland und dem deutschen Nordsee-Sektor. Strukturen, Strukturentwicklung, Paläogeographie, Geol. Jahrb., A 153, 1–88, 3 CD–ROMs, 2001.

Best, G.: Floßtektonik in Norddeutschland: Erste Ergebnisse reflexionsseismischer Untersuchungen an der Salzstruktur "Oberes Allertal", Z. Dtsch. Geol. Ges., 147, 455–464, 1996.

Best, G., Kockel, F., and Schöneich, H.: Geological history of the southern Horn Graben, Geol. Mijnbouw, 62, 25–33, 1983.

Bishop, D. J., Buchanan, P. G., and Bishop, C. J.: Gravity-driven thin-skinned extension above Zechstein Group evaporites in the western central North Sea: an application of computer-aided section restoration techniques, Mar. Pet. Geol., 12, 115–135, https://doi.org/10.1016/0264-8172(95)92834-J, 1995.

Bodego, A. and Agirrezabala, L. M.: Syn-depositional thin-and thick-skinned extensional tectonics in the mid-Cretaceous Lasarte sub-basin, western Pyrenees, Basin Research, 25, 594–612, https://doi.org/https://doi.org/10.1111/bre.12017, 2013.

Bonini, M., Sani, F., and Antonielli, B.: Basin inversion and contractional reactivation of inherited normal faults: A review based on previous and new experimental models, Tectonophysics, 522, 55–88, https://doi.org/10.1016/j.tecto.2011.11.014, 2012.

Brun, J.-P. and Fort, X.: Salt tectonics at passive margins: Geology versus models, Mar. Pet. Geol., 28, 1123–1145, https://doi.org/10.1016/j.marpetgeo.2011.03.004, 2011.

Brun, J.-P. and Mauduit, T. P.-O.: Salt rollers: structure and kinematics from analogue modelling, Mar. Pet. Geol., 26, 249–258, https://doi.org/10.1016/j.marpetgeo.2008.02.002, 2009.

Buchanan, P. G., Bishop, D. J., and Hood, D. N.: Development of salt-related structures in the Central North Sea: results from section balancing, Geol. Soc. Lond., Spec. Pub., 100, 111–128, https://doi.org/10.1144/GSL.SP.1996.100.01.09, 1996.

Burliga, S., Koyi, H. A., and Chemia, Z.: Analogue and numerical modelling of salt supply to a diapiric structure rising above an active basement fault, Geol. Soc. Lond., Spec. Pub., 363, 395–408, https://doi.org/10.1144/SP363.18, 2012.

Byerlee, J.: Friction of rocks, Pure and applied geophysics, 116, 615–626, https://doi.org/10.1007/978-3-0348-7182-2_4, 1978.

Cámara, P.: Inverted turtle salt anticlines in the eastern Basque-Cantabrian basin, Spain, Marine and Petroleum Geology, 117, 104 358, https://doi.org/10.1016/j.marpetgeo.2020.104358, 2020.

Cartwright, J. A., Stewart, S., and Clark, J.: Salt dissolution and salt-related deformation of the Forth Approaches Basin, UK North Sea, Mar. Pet. Geol., 18, 757–778, https://doi.org/10.1016/S0264-8172(01)00019-8, 2001.

Chapman, T. J.: The Permian to Cretaceous structural evolution of the Western Approaches Basin (Melville sub-basin), UK, in: Inversion Tectonics, vol. 44, pp. 177–200, Geological Society of London, https://doi.org/https://doi.org/10.1144/GSL.SP.1989.044.01.11, 1989.

Clark, J. A., Stewart, S. A., and Cartwright, J. A.: Evolution of the NW margin of the North Permian Basin, UK North Sea, J. Geol. Soc., 155, 663–676, https://doi.org/10.1144/gsjgs.155.4.0663, 1998.

Clausen, O. R. and Pedersen, P. K.: Late Triassic structural evolution of the southern margin of the Ringkøbing-Fyn High, Denmark, Mar. Pet. Geol., 16, 653–665, https://doi.org/10.1016/S0264-8172(99)00026-4, 1999.

Clausen, O. R., Andresen, K. J., Mauritzen, E. K., Connolly, D., and Korstgård, J. A.: Hanging-wall deformation and gas-migration associated to a major salt detaching fault in the Norwegian Danish Basin, Journal of Structural Geology, 79, 90–109, https://doi.org/10.1016/j.jsg.2015.08.003, 2015.

Coleman, A. J., Jackson, C. A.-L., and Duffy, O. B.: Balancing sub-and supra-salt strain in salt-influenced rifts: Implications for extension estimates, J. Struct. Geol., 102, 208–225, 2017.

Coward, M. and Stewart, S.: Salt-influenced structures in the Mesozoic-Tertiary cover of the southern North Sea, UK, in: Salt tectonics; a global perspective, edited by Jackson, M. P. A., Roberts, D. G., and Snelson, S., vol. 65, pp. 229–250, American Association of Petroleum Geologists, 1995.

Dadlez, R., Narkiewicz, M., Stephenson, R. A., Visser, M. T. M., and Van Wees, J. D.: Tectonic evolution of the Mid-Polish Trough: modelling implications and significance for central European geology, Tectonophysics, 252, 179–195, https://doi.org/10.1016/0040-1951(95)00104-2, 1995.

Dahlen, F. A.: Critical taper model of fold-and-thrust belts and accretionary wedges, Annual Review of Earth and Planetary Sciences, 18, 55, 1990.

Dancer, P. N., Algar, S. T., and Wilson, I. R.: Structural evolution of the Slyne Trough, in: Petroleum Geology of Northwest Europe: Proceedings of the 5th Conference, vol. 5, pp. 445–453, Geological Society, London, 1999.

Davy, P. and Cobbold, P. R.: Experiments on shortening of a 4-layer model of the continental lithosphere, Tectonophysics, 188, 1–25, 1991.

Dooley, T. P. and Hudec, M. R.: Extension and inversion of salt-bearing rift systems, Solid Earth, 11, 1187–1204, https://doi.org/https://doi.org/10.5194/se-11-1187-2020, 2020.

Dooley, T. P., McClay, K. R., and Pascoe, R.: 3D analogue models of variable displacement extensional faults: applications to the Revfallet Fault system, offshore mid-Norway, Geol. Soc. Lond., Spec. Pub., 212, 151–167, https://doi.org/10.1144/GSL.SP.2003.212.01.10, 2003.

Dooley, T. P., McClay, K. R., Hempton, M., and Smit, D.: Salt tectonics above complex basement extensional fault systems: results from analogue modelling, in: Geological Society, London, Petroleum Geology Conference series, vol. 6, pp. 1631–1648, Geological Society of London, https://doi.org/10.1144/0061631, 2005.

Dooley, T. P., Hudec, M. R., Carruthers, D., Jackson, M. P. A., and Luo, G.: The effects of base-salt relief on salt flow and suprasalt deformation patterns–Part 1: Flow across simple steps in the base of salt, Interpretation, 5, SD1–SD23, https://doi.org/https://doi.org/10.1190/INT-2016-0087.1, 2017.

Duffy, O. B., Gawthorpe, R. L., Docherty, M., and Brocklehurst, S. H.: Mobile evaporite controls on the structural style and evolution of rift basins: Danish Central Graben, North Sea, Basin Res., 25, 310–330, https://doi.org/10.1111/bre.12000, 2013.

England, P. and McKenzie, D.: A thin viscous sheet model for continental deformation, Geophysical Journal International, 70, 295–321, https://doi.org/10.1111/j.1365-246X.1982.tb04969.x, 1982.

Ferrer, O., Roca, E., Benjumea, B., Muñoz, J. A., Ellouz, N., Team, M., et al.: The deep seismic reflection MARCONI-3 profile: Role of extensional Mesozoic structure during the Pyrenean contractional deformation at the eastern part of the Bay of Biscay, Marine and Petroleum Geology, 25, 714–730, https://doi.org/https://doi.org/10.1016/j.marpetgeo.2008.06.002, 2008.

Ferrer, O., Jackson, M. P. A., Roca, E., and Rubinat, M.: Evolution of salt structures during extension and inversion of the Offshore Parentis Basin (Eastern Bay of Biscay), Geol. Soc. Lond., Spec. Pub., 363, 361–380, https://doi.org/10.1144/SP363.16, 2012.

Ferrer, O., Roca, E., and Vendeville, B.: The role of salt layers in the hangingwall deformation of kinked-planar extensional faults: Insights from 3D analogue models and comparison with the Parentis Basin, Tectonophysics, 636, 338–350, https://doi.org/10.1016/j.tecto.2014.09.013, 2014.

Fort, X., Brun, J.-P., and Chauvel, F.: Salt tectonics on the Angolan margin, synsedimentary deformation processes, AAPG Bull., 88, 1523–1544, 2004.

Ge, H., Jackson, M. P. A., and Vendeville, B. C.: Kinematics and dynamics of salt tectonics driven by progradation, AAPG Bull., 81, 398–423, 1997.

Ge, Z., Gawthorpe, R. L., Rotevatn, A., and Thomas, M. B.: Impact of normal faulting and pre-rift salt tectonics on the structural style of salt-influenced rifts: The Late Jurassic Norwegian Central Graben, North Sea, Basin Res., 29, 674–698, https://doi.org/https://doi.org/10.1111/bre.12219, 2017.

Ge, Z., Warsitzka, M., Rosenau, M., and Gawthorpe, R. L.: Progressive tilting of salt-bearing continental margins controls thin-skinned deformation, Geology, 47, 1122–1126, https://doi.org/10.1130/G46485.1, 2019.

Geil, K.: The development of salt structures in Denmark and adjacent areas: the role of basin floor dip and differential pressure, First Break, 9, https://doi.org/10.3997/1365-2397.1991022, 1991.

Geluk, M. C.: Stratigraphy and tectonics of Permo-Triassic basins in the Netherlands and surrounding areas, Ph.D. thesis, Utrecht University, 2005.

Heaton, R. C., Jackson, M. P. A., Bamahmoud, M., and Nani, A. S. O.: Superposed Neogene extension, contraction, and salt canopy emplacement in the Yemeni Red Sea, in: Salt tectonics: a global perspective, edited by Jackson, M. P. A., Roberts, D. G., and Snelson, S., vol. 65, pp. 333–351, AAPG Mem., 1995.

Hodgson, N. A., Farnsworth, J., and Fraser, A. J.: Salt-related tectonics, sedimentation and hydrocarbon plays in the Central Graben, North Sea, UKCS, Geol. Soc. Lond., Spec. Pub., 67, 31–63, 1992.

Høiland, O., Kristensen, J., and Monsen, T.: Mesozoic evolution of the Jæren High area, Norwegian Central North Sea, in: Petroleum Geology of Northwest Europe: Proceedings of the 4th Conference, vol. 4, pp. 1189–1195, The Geological Society, London, Geological Society, London, https://doi.org/https://doi.org/10.1144/0041189, 1993.

Hubbert, M. K.: Theory of scale models as applied to the study of geologic structures, Geological Society of America Bulletin, 48, 1459–1520, 1937.

Hudec, M. R. and Jackson, M. P. A.: Terra infirma: understanding salt tectonics, Earth-Science Reviews, 82, 1–28, https://doi.org/10.1016/j.earscirev.2007.01.001, 2007.

Hudec, M. R., Jackson, M. P. A., and Schultz-Ela, D. D.: The Paradox of Minibasin Subsidence into Salt, Geological Society of America Bulletin, 121, 201–221, https://doi.org/10.1130/B26275.1, 2009.

Hughes, M. and Davison, I.: Geometry and growth kinematics of salt pillows in the southern North Sea, Tectonophysics, 228, 239–254, 1993.

Jackson, C. A.-L. and Lewis, M. M.: Structural style and evolution of a salt-influenced rift basin margin; the impact of variations in salt composition and the role of polyphase extension, Basin Research, 28, 81–102, https://doi.org/10.1111/bre.12099, 2016.

Jackson, C. A.-L., Jackson, M. P. A., and Hudec, M. R.: Understanding the kinematics of salt-bearing passive margins: A critical test of competing hypotheses for the origin of the Albian Gap, Santos Basin, offshore Brazil, GSA Bulletin, 127, 1730–1751, https://doi.org/10.1130/B31290.1, 2015.

Jackson, M. P. A. and Cramez, C.: Seismic recognition of salt welds in salt tectonics regimes, in: Gulf of Mexico salt tectonics, associated processes and exploration potential: Gulf Coast Section SEPM Foundation, 10th Annual Research Conference, pp. 66–71, SEPM Society for Sedimentary Geology, https://doi.org/10.5724/gcs.89.10.0066, 1989.

Jackson, M. P. A. and Hudec, M. R.: Salt Tectonics: Principles and Practice, Cambridge University Press, 2017.

Jackson, M. P. A. and Talbot, C. J.: External shapes, strain rates, and dynamics of salt structures, Geological Society of America Bulletin, 97, 305–323, https://doi.org/10.1130/0016-7606(1986)97<305:ESSRAD>2.0.CO;2, 1986.

Jaeger, J. C., Cook, N. G. W., and Zimmerman, R.: Fundamentals of Rock Mechanics, Blackwell Publishing, 4 edn., 2007.

Jammes, S., Manatschal, G., Lavier, L., and Masini, E.: Tectonosedimentary evolution related to extreme crustal thinning ahead of a propagating ocean: Example of the western Pyrenees, Tectonics, 28, https://doi.org/10.1029/2008TC002406, 2009.

Jammes, S., Manatschal, G., and Lavier, L.: Interaction between prerift salt and detachment faulting in hyperextended rift systems: The example of the Parentis and Mauléon basins (Bay of Biscay and western Pyrenees), AAPG Bulletin, 94, 957–975, https://doi.org/10.1306/12090909116, 2010.

Jensen, L. and Sørensen, K.: Tectonic framework and halokinesis of the Nordkapp Basin, Barents Sea, in: Structural and Tectonic Modelling and its Application to Petroleum Geology, edited by Larsen, R. M., Brekke, H., Larsen, B. T., and Talleraas, E., vol. 1, pp. 109–120, Elsevier, https://doi.org/10.1016/B978-0-444-88607-1.50012-7, 1992.

Kockel, F. e., (mit Beiträgen von Baldschuhn, R., Best, G., Binot, F., Frisch, U., Gross, U., Jürgens, U., Röhling, H.-G., and Sattler-Kosinowski, S.: Structural and Palaeogeographical Development of the German North Sea Sector, Beitr. reg. Geol. Erde, 26, 96 pp., 1995.

Koyi, H., Jenyon, M. K., and Petersen, K.: The effect of basement faulting on diapirism, Journal of Petroleum Geology, 16, 285–312, https://doi.org/10.1111/j.1747-5457.1993.tb00339.x, 1993.

Koyi, H., Talbot, C. J., and Torudbakken, B. O.: Salt tectonics in the northeastern Nordkapp Basin, southwestern Barents Sea, AAPG Mem., 65, 437–447, 1995.

Krzywiec, P.: Triassic evolution of the Kłodawa salt structure: basement-controlled salt tectonics within the Mid-Polish Trough (Central Poland), Geological Quarterly, 48, 123–134, 2004.

Krzywiec, P.: Triassic-Jurassic evolution of the Pomeranian segment of the Mid-Polish Trough – basement tectonics and subsidence patterns, Geological Quarterly, 50, 139–150, 2006a.

Krzywiec, P.: Structural inversion of the Pomeranian and Kuiavian segments of the Mid-Polish Trough – lateral variations in timing and structural style, Geological Quarterly, 50, 151–168, 2006b.

Krzywiec, P.: Mesozoic and Cenozoic evolution of salt structures within the Polish basin: An overview, Geol. Soc. Lond., Spec. Pub., 363, 381–394, https://doi.org/10.1144/SP363.17, 2012.

Krzywiec, P., Peryt, T. M., Kiersnowski, H., Pomianowski, P., Czapowski, G., and Kwolek, K.: Permo-Triassic Evaporites of the Polish Basin and Their Bearing on the Tectonic Evolution and Hydrocarbon System, an Overview, in: Permo-Triassic Salt Provinces of Europe, North

Africa and the Atlantic Margins, edited by Soto, J. I., Flinch, J. F., and Tari, G., pp. 243–261, Elsevier, Amsterdam, Netherlands, 1st edn., https://doi.org/10.1016/B978-0-12-809417-4.00012-4, 2017.

Kusznir, N. J., Stovba, S. M., Stephenson, R. A., and Poplavskii, K. N.: The formation of the northwestern Dniepr-Donets Basin: 2-D forward and reverse syn-rift and post-rift modelling, Tectonophysics, 268, 237–255, https://doi.org/10.1016/S0040-1951(96)00230-2, 1996.

Labaume, P. and Teixell, A.: Evolution of salt structures of the Pyrenean rift (Chaînons Béarnais, France): From hyper-extension to tectonic inversion, Tectonophysics, in press, 228 451, https://doi.org/10.1016/j.tecto.2020.228451, 2020.

Lagabrielle, Y., Labaume, P., and de Saint Blanquat, M.: Mantle exhumation, crustal denudation, and gravity tectonics during Cretaceous rifting in the Pyrenean realm (SW Europe): Insights from the geological setting of the lherzolite bodies, Tectonics, 29, https://doi.org/10.1029/2009TC002588, 2010.

LaVision, A.: StrainMaster Manual for DaVis 10.0., LaVision GmbH, Goettingen, 2018.

Lewis, M. M., Jackson, C. A.-L., and Gawthorpe, R. L.: Salt-influenced normal fault growth and forced folding: The Stavanger Fault System, North Sea, Journal of Structural Geology, 54, 156–173, https://doi.org/10.1016/j.jsg.2013.07.015, 2013.

Lohrmann, J., Kukowski, N., Adam, J., and Oncken, O.: The impact of analogue material properties on the geometry, kinematics, and dynamics of convergent sand wedges, J. Struct. Geol., 25, 1691–1711, https://doi.org/10.1016/S0191-8141(03)00005-1, 2003.

Loncke, L., Vendeville, B. C., Gaullier, V., and Mascle, J.: Respective contributions of tectonic and gravity-driven processes on the structural pattern in the Eastern Nile deep-sea fan: insights from physical experiments, Basin Research, 22, 765–782, https://doi.org/https://doi.org/10.1111/j.1365-2117.2009.00436.x, 2010.

López-Mir, B., Muñoz, J. A., and García-Senz, J.: Extensional salt tectonics in the partially inverted Cotiella post-rift basin (south-central Pyrenees): structure and evolution, International Journal of Earth Sciences, 104, 419–434, https://doi.org/10.1007/s00531-014-1091-9, 2015.

Lymer, G., Vendeville, B. C., Gaullier, V., Chanier, F., and Gaillard, M.: Using salt tectonic structures as proxies to reveal post-rift crustal tectonics: The example of the Eastern Sardinian margin (Western Tyrrhenian Sea), Marine and Petroleum Geology, pp. 214–231, 2018.

Martín-Martín, J., Vergés, J., Saura, E., Moragas, M., Messager, G., Baqués, V., Razin, P., Grélaud, C., Malaval, M., Joussiaume, R., et al.: Diapiric growth within an Early Jurassic rift basin: The Tazoult salt wall (central High Atlas, Morocco), Tectonics, 36, 2–32, https://doi.org/10.1002/2016TC004300, 2017.

Mauduit, T., Guerin, G., Brun, J.-P., and Lecanu, H.: Raft tectonics: the effects of basal slope angle and sedimentation rate on progressive extension, Journal of Structural Geology, 19, 1219–1230, https://doi.org/10.1016/S0191-8141(97)00037-0, 1997.

Maystrenko, Y. P., Bayer, U., and Scheck-Wenderoth, M.: Structure and evolution of the Glueckstadt Graben due to salt movements, Int. J. Earth Science, 94, 799–814, https://doi.org/10.1007/s00531-005-0003-4, 2005.

Maystrenko, Y. P., Bayer, U., and Scheck-Wenderoth, M.: Structure and Evolution of the Glueckstadt Graben in Relation to the Other PostPermian Subbasins of the Central European Basin System, in: Permo-Triassic Salt Provinces of Europe, North Africa and the Atlantic Margins, edited by Soto, J. I., Flinch, J. F., and Tari, G., pp. 203–220, Elsevier, Amsterdam, Netherlands, 1st edn., https://doi.org/10.1016/B978-0-12-809417-4.00010-0, 2017.

Mianaekere, V. and Adam, J.: 'Halo-kinematic'sequence-stratigraphic analysis of minibasins in the deepwater contractional province of the Liguro-Provençal basin, Western Mediterranean, Marine and Petroleum Geology, p. 104307, https://doi.org/https://doi.org/10.1016/j.marpetgeo.2020.104307, 2020.

Mitchell, D. J. W., Allen, R. B., Salama, W., and Abouzakm, A.: Tectonostratigraphic framework and hydrocarbon potential of the Red Sea, Journal of Petroleum Geology, 15, 187–210, https://doi.org/10.1111/j.1747-5457.1992.tb00962.x, 1992.

Mohr, M., Kukla, P. A., Urai, J., and Bresser, G.: Multiphase salt tectonic evolution in NW Germany: seismic interpretation and retro-deformation, Int. J. Earth Science, 94, 917–940, 2005.

Moragas, M., Vergés, J., Nalpas, T., Saura, E., Martín-Martín, J. D., Messager, G., and Hunt, D. W.: The impact of syn-and post-extension prograding sedimentation on the development of salt-related rift basins and their inversion: Clues from analogue modelling, Marine and Petroleum Geology, 88, 985–1003, 2017.

Mukherjee, S., Talbot, C. J., and Koyi, H. A.: Viscosity estimates of salt in the Hormuz and Namakdan salt diapirs, Persian Gulf, Geological Magazine, 147, 497–507, https://doi.org/10.1017/S001675680999077X, 2010.

Nalpas, T. and Brun, J.-P.: Salt flow and diapirism related to extension at crustal scale, Tectonophysics, 228, 349–362, https://doi.org/10.1016/0040-1951(93)90348-N, 1993.

Nilsen, K. T., Johansen, J. T., and Vendeville, B. C.: Influence of regional tectonics on halokinesis in the Nordkapp Basin, Barents Sea, in: Salt tectonics: a global perspective, edited by Jackson, M. P. A., Roberts, D. G., and Snelson, S., 65, pp. 413–436, AAPG Mem., 1996.

Panien, M., Schreurs, G., and Pfiffner, A.: Mechanical behaviour of granular materials used in analogue modelling: insights from grain characterisation, ring-shear tests and analogue experiments, J. Struct. Geol., 28, 1710–1724, https://doi.org/10.1016/j.jsg.2006.05.004, 2006.

Pascoe, R., Hooper, R., Storhaug, K., and Harper, H.: Evolution of extensional styles at the southern termination of the Nordland Ridge, Mid-Norway: a response to variations in coupling above Triassic salt, in: Geological Society, London, Petroleum Geology Conference Series, vol. 5, pp. 83–90, Geological Society of London, London, https://doi.org/10.1144/0050083, 1999.

Peel, F. J.: The engines of gravity-driven movement on passive margins: Quantifying the relative contribution of spreading vs. gravity sliding mechanisms, Tectonophysics, 633, 126–142, https://doi.org/10.1016/j.tecto.2014.06.023, 2014.

Pena dos Reis, R., Pimentel, N., Fainstein, R., Reis, M., and Rasmussen, B.: Influence of Salt Diapirism on the Basin Architecture and Hydrocarbon Prospects of the Western Iberian Margin, in: Permo-Triassic Salt Provinces of Europe, North Africa and the Atlantic Margins, edited by Soto, J. I., Flinch, J. F., and Tari, G., pp. 313–329, Elsevier, https://doi.org/10.1016/B978-0-12-809417-4.00015-X, 2017.

Penge, J., Munns, J. W., Taylor, B., and Windle, T. M. F.: Rift–raft tectonics: examples of gravitational tectonics from the Zechstein basins of northwest Europe, in: Geological Society, London, Petroleum Geology Conference series, edited by Fleet, A. J. and Boldy, S. A. R., vol. 5, pp. 201–213, Geological Society, London, 1999.

Pollard, D., Pollard, D. D., Fletcher, R. C., and Fletcher, R. C.: Fundamentals of Structural Geology, Cambridge University Press, 2005.

Quirk, D. G., Schødt, N., Lassen, B., Ings, S. J., Hsu, D., Hirsch, K. K., and Von Nicolai, C.: Salt tectonics on passive margins: examples from Santos, Campos and Kwanza basins, Geological Society, London, Special Publications, 363, 207–244, https://doi.org/10.1144/SP363.10, 2012.

Radies, D., Stollhofen, H., Hollmann, G., and Kukla, P.: Synsedimentary faults and amalgamated unconformities: insights from 3D-seismic and core analysis of the Lower Triassic Middle Buntsandstein, Ems Trough, north-western Germany, Int. J. Earth Science, 94, 863–875, 2005.

Ramberg, H.: Gravity, Deformation and the Earth's Crust: in Theory, Experiments and Geological Application, Academic Press, London, 1981.

Rasmussen, E. S., Lomholt, S., Andersen, C., and Vejbæk, O. V.: Aspects of the structural evolution of the Lusitanian Basin in Portugal and the shelf and slope area offshore Portugal, Tectonophysics, 300, 199–225, https://doi.org/10.1016/S0040-1951(98)00241-8, 1998.

Rojo, L. A., Cardozo, N., Escalona, A., and Koyi, H.: Structural style and evolution of the Nordkapp Basin, Norwegian Barents Sea, AAPG Bulletin, 103, 2177–2217, https://doi.org/https://doi.org/10.1306/01301918028, 2019.

https://doi.org/10.5194/se-2021-17
Preprint. Discussion started: 25 February 2021

Rojo, L. A., Koyi, H., Cardozo, N., and Escalona, A.: Salt tectonics in salt-bearing rift basins: Progradational loading vs extension, Journal of Structural Geology, 141, 104 193, https://doi.org/https://doi.org/10.1016/j.jsg.2020.104193, 2020.

Rowan, M. G. and Lindsø, S.: Salt tectonics of the Norwegian Barents Sea and northeast Greenland shelf, in: Permo-Triassic Salt Provinces of Europe, North Africa and the Atlantic Margins, edited by Soto, J. I., Flinch, J. F., and Tari, G., pp. 265–286, Elsevier, https://doi.org/https://doi.org/10.1016/B978-0-12-809417-4.00013-6, 2017.

Rowan, M. G., Peel, F. J., and Vendeville, B. C.: Gravity-driven fold belts on passive margins, in: Thrust tectonics and hydrocarbon systems, edited by McCLay, K. R., vol. 82, pp. 157–182, AAPG Mem., 2004.

Rowan, M. G., Peel, F. J., Vendeville, B. C., and Gaullier, V.: Salt tectonics at passive margins: Geology versus models – Discussion, Mar. Pet. Geol., 37, 184–194, 2012.

Rudolf, M., Boutelier, D., Rosenau, M., Schreurs, G., and Oncken, O.: Rheological benchmark of silicone oils used for analog modeling of short-and long-term lithospheric deformation, Tectonophysics, 2015.

Rudolf, M., Boutelier, D., Rosenau, M., Schreurs, G., and Oncken, O.: Rheological benchmark of silicone oils used for analog modeling of short-and long-term lithospheric deformation, Tectonophysics, 684, 12–22, https://doi.org/10.1016/j.tecto.2015.11.028, 2016.

Saspiturry, N., Razin, P., Baudin, T., Serrano, O., Issautier, B., Lasseur, E., Allanic, C., Thinon, I., and Leleu, S.: Symmetry vs. asymmetry of a hyper-thinned rift: example of the Mauléon Basin (Western Pyrenees, France), Marine and Petroleum Geology, 104, 86–105, 2019.

Saura, E., Ardèvol i Oró, L., Teixell, A., and Vergés, J.: Rising and falling diapirs, shifting depocenters, and flap overturning in the Cretaceous Sopeira and Sant Gervàs subbasins (Ribagorça Basin, southern Pyrenees), Tectonics, 35, 638–662, 2016.

Schléder, Z., Urai, J. L., Nollet, S., and Hilgers, C.: Solution-precipitation creep and fluid flow in halite: a case study of Zechstein (Z1) rocksalt from Neuhof salt mine (Germany), Int. J. Earth Science, 97, 1045–1056, 2008.

Schueller, S. and Davy, P.: Gravity influenced brittle-ductile deformation and growth faulting in the lithosphere during collision: Results from laboratory experiments, Journal of Geophysical Research: Solid Earth, 113, https://doi.org/10.1029/2007JB005560, 2008.

Schultz-Ela, D. D.: Excursus on gravity gliding and gravity spreading, J. Struct. Geol., 23, 725–731, 2001.

Seni, S. J. and Jackson, M. P. A.: Sedimentary Record of Cretaceous and Tertiary Salt Movement, East Texas Basin: Times, Rates, and Volumes of Salt Flow and Their Implications for Nuclear Waste Isolation and Petroleum Exploration, in: The University of Texas at Austin Bureau of Economic Geology Report of Invesitgations, vol. 139, p. 89 pp., Bureau of Economic Geology, University of Texas of Austin, 1984.

Sornette, A., Davy, P., and Sornette, D.: Fault growth in brittle-ductile experiments and the mechanics of continental collisions, Journal of Geophysical Research: Solid Earth, 98, 12 111–12 139, https://doi.org/10.1029/92JB01740, 1993.

Stewart, S. A.: Salt tectonics in the North Sea Basin: a structural style template for seismic interpreters, Geol. Soc. Lond., Spec. Pub., 272, 361–396, 2007.

Stewart, S. A. and Clark, J. A.: Impact of salt on the structure of the Central North Sea hydrocarbon fairways, Geological Society, London, Petroleum Geology Conference series, 5, 179–200, https://doi.org/10.1144/0050179, 1999.

Stewart, S. A. and Coward, M. P.: Synthesis of salt tectonics in the southern North Sea, UK, Mar. Pet. Geol., 12, 457–475, 1995.

Stovba, S. M. and Stephenson, R. A.: Style and timing of salt tectonics in the Dniepr-Donets Basin (Ukraine): implications for triggering and driving mechanisms of salt movement in sedimentary basins, Mar. Pet. Geol., 19, 1169–1189, https://doi.org/10.1016/S0264-8172(03)00023-0, 2003.

Stovba, S. M., Stephenson, R. A., and Kivshik, M.: Structural features and evolution of the Dniepr-Donets Basin, Ukraine, from regional seismic reflection profiles, Tectonophysics, 268, 127–147, https://doi.org/10.1016/S0040-1951(96)00222-3, 1996.

Strozyk, F., Urai, J. L., van Gent, H., de Keijzer, M., and Kukla, P. A.: Regional variations in the structure of the Permian Zechstein 3 intrasalt stringer in the northern Netherlands: 3D seismic interpretation and implications for salt tectonic evolution, Interpretation, 2, SM101–SM117, 2014.

Strozyk, F., Reuning, L., Scheck-Wenderoth, M., and Tanner, D. C.: The tectonic history of the Zechstein Basin in the Netherlands and Germany, in: Permo-Triassic Salt Provinces of Europe, North Africa and the Atlantic Margins, edited by Soto, J. I., Flinch, J. F., and Tari, G., pp. 221–241, Elsevier, Amsterdam, Netherlands, 1st edn., https://doi.org/10.1016/B978-0-12-809417-4.00011-2, 2017.

Tanveer, M. and Korstgård, J. A.: Structural evolution of the Feda Graben area–A new model, Mar. Pet. Geol., 26, 990–999, https://doi.org/10.1016/j.marpetgeo.2008.04.010, 2009.

Ten Veen, J. H., Van Gessel, S. F., and Den Dulk, M.: Thin-and thick-skinned salt tectonics in the Netherlands; a quantitative approach, Neth. J. Geosci./ Geol.Mijn., 91, 447–464, https://doi.org/10.1017/S0016774600000330, 2012.

Thieme, B. and Rockenbauch, K.: Flosstektonik in der Trias der deutschen südlichen Nordsee, Erdöl, Erdgas, Kohle, 117, 568–573, 2001.

Thomas, D. W. and Coward, M. P.: Mesozoic regional tectonics and South Viking Graben formation: evidence for localized thin-skinned detachments during rift development and inversion, Marine and Petroleum Geology, 13, 149–177, https://doi.org/10.1016/0264-8172(95)00034-8, 1996.

Troudi, H., Tari, G., Alouani, W., and Cantarella, G.: Styles of salt tectonics in Central Tunisia: an overview, in: Permo-Triassic Salt Provinces of Europe, North Africa and the Atlantic Margins, edited by Soto, J. I., Flinch, J. F., and Tari, G., pp. 543–561, Elsevier, https://doi.org/10.1016/B978-0-12-809417-4.00026-4, 2017.

Turcotte, D. L. and Schubert, G.: Geodynamics, Cambridge University Press, third edn., 2014.

Tvedt, A. B. M., Rotevatn, A., Jackson, C. A.-L., Fossen, H., and Gawthorpe, R. L.: Growth of normal faults in multilayer sequences: a 3D seismic case study from the Egersund Basin, Norwegian North Sea, J. Struct. Geol., 55, 1–20, https://doi.org/10.1016/j.jsg.2013.08.002, 2013.

Tvedt, A. B. M., Rotevatn, A., and Jackson, C. A. L.: Supra-salt normal fault growth during the rise and fall of a diapir: Perspectives from 3D seismic reflection data, Norwegian North Sea, Journal of Structural Geology, 91, 1–26, 2016.

Urai, J. L., Schléder, Z., Spiers, C. J., and Kukla, P. A.: Flow and Transport Properties of Salt Rocks, in: Dynamics of Complex Intracontinental Basins: The Central European Basin System, edited by Littke, R., Bayer, U., Gajewski, D., and Nelskamp, S., pp. 277–290, Springer-Verlag, Berlin, Heidelberg, 2008.

Vackiner, A. A., Antrett, P., Strozyk, F., Back, S., Kukla, P., and Stollhofen, H.: Salt kinematics and regional tectonics across a Permian gas field: a case study from East Frisia, NW Germany, Int. J. Earth Science, 102, 1701–1716, https://doi.org/10.1007/s00531-013-0887-3, 2013.

Van Gent, H., Urai, J. L., and De Keijzer, M.: The internal geometry of salt structures – A first look using 3D seismic data from the Zechstein of the Netherlands, J. Struct. Geol., 33, 292–311, https://doi.org/10.1016/j.jsg.2010.07.005, 2011.

Van Keken, P. E., Spiers, C. J., Van den Berg, A. P., and Muyzert, E. J.: The effective viscosity of rocksalt: implementation of steady-state creep laws in numerical models of salt diapirism, Tectonophysics, 225, 457–476, https://doi.org/10.1016/0040-1951(93)90310-G, 1993.

Van Winden, M., de Jager, J., Jaarsma, B., and Bouroullec, R.: New insights into salt tectonics in the northern Dutch offshore: a framework for hydrocarbon exploration, in: Mesozoic Resource Potential in the Southern Permian Basin, edited by Kilhams, B., Kukla, P. A., Mazur, S., McKie, T., Mijnlieff, H. F., and Van Ojik, K., vol. 469, pp. 99–117, Geol. Soc. (Lond.) Spec. Publ., https://doi.org/10.1144/SP469.9, 2018.

Vejbæk, O. V.: The Horn Graben, and its relationship to the Oslo Graben and the Danish Basin, Tectonophysics, 178, 29–49, 1990.

Vendeville, B. C.: Salt tectonics driven by sediment progradation: Part I – Mechanics and kinematics, AAPG Bull., 89, 1071–1079, 2005.

Vendeville, B. C., Ge, H., and Jackson, M. P. A.: Scale models of salt tectonics during basement-involved extension, Petroleum Geoscience, 1, 179–183, https://doi.org/10.1144/petgeo.1.2.179, 1995.

Vergés, J., Moragas, M., Martín-Martín, J. D., Saura, E., Casciello, E., Razin, P., Grélaud, C., Malaval, M., Joussiame, R., Messager, G., et al.: Salt tectonics in the Atlas mountains of Morocco, in: Permo-Triassic Salt Provinces of Europe, North Africa and the Atlantic Margins, edited by Soto, J. I., Flinch, J. F., and Tari, G., pp. 563–579, Elsevier, https://doi.org/10.1016/B978-0-12-809417-4.00027-6, 2017.

Wagner, R., Leszczyński, K., Pokorski, J., and Gumulak, K.: Palaeotectonic cross-sections through the Mid-Polish Trough, Geological Quarterly, 46, 293–306, 2002.

Walker, I. M. and Cooper, W. G.: The structural and stratigraphic evolution of the northeast margin of the Sole Pit Basin, in: Proceedings of the 3rd Conference on Petroleum geology of North West Europe, edited by Brooks, J. and Glennie, K. W., vol. 1, pp. 263–275, Graham & Trotman, London, 1987.

Warsitzka, M., Kley, J., and Kukowski, N.: Analogue experiments of salt flow and pillow growth due to basement faulting and differential loading, Solid Earth, 6, 9–31, https://doi.org/10.5194/sed-6-1625-2014, 2015.

Warsitzka, M., Kley, J., Jähne-Klingberg, F., and Kukowski, N.: Dynamics of prolonged salt movement in the Glückstadt Graben (NW Germany) driven by tectonic and sedimentary processes, Int. J. Earth Science, 106, 131–155, https://doi.org/10.1007/s00531-016-1306-3, 2017.

Warsitzka, M., Kukowski, N., and Kley, J.: Salt flow direction and velocity during subsalt normal faulting and syn-kinematic sedimentation – implications from analytical calculations, Geophysical Journal International, 213, 115–134, https://doi.org/10.1093/gji/ggx552, 2018.

Warsitzka, M., Závada, P., Pohlenz, A., and Rosenau, M.: Ring-shear test data of quartz sand used for analogue experiments in the laboratory of the Institute of Geophysics of the Czech Academy of Science, https://doi.org/10.5880/GFZ.4.1.2019.008, 2019.

Watts, A. B., Karner, G., and Steckler, M. S.: Lithospheric flexure and the evolution of sedimentary basins, Philosophical Transactions of the Royal Society of London. Series A, Mathematical and Physical Sciences, 305, 249–281, https://doi.org/10.1098/rsta.1982.0036, 1982.

Weijermars, R. and Schmeling, H.: Scaling of Newtonian and non-Newtonian fluid dynamics without inertia for quantitative modelling of rock flow due to gravity (including the concept of rheological similarity), Physics of the Earth and Planetary Interiors, 43, 316–330, https://doi.org/10.1016/0031-9201(86)90021-X, 1986.

Weijermars, R., Jackson, M. P. A., and Vendeville, B. C.: Rheological and tectonic modeling of salt provinces, Tectonophysics, 217, 143–174, https://doi.org/10.1016/0040-1951(93)90208-2, 1993.

Withjack, M. O. and Callaway, S.: Active normal faulting beneath a salt layer: an experimental study of deformation patterns in the cover sequence, AAPG Bull., 84, 627–651, https://doi.org/10.1306/C9EBCE73-1735-11D7-8645000102C1865D, 2000.

Wong, T. E., Batjes, D. A. J., de Jager, J., and van Wetenschappen, K. N. A.: Geology of the Netherlands, Amsterdam : Royal Netherlands Academy of Arts and Sciences, 2007.

Zoback, M. L. and Mooney, W. D.: Lithospheric buoyancy and continental intraplate stresses, International Geology Review, 45, 95–118, https://doi.org/10.2747/0020-6814.45.2.95, 2003.

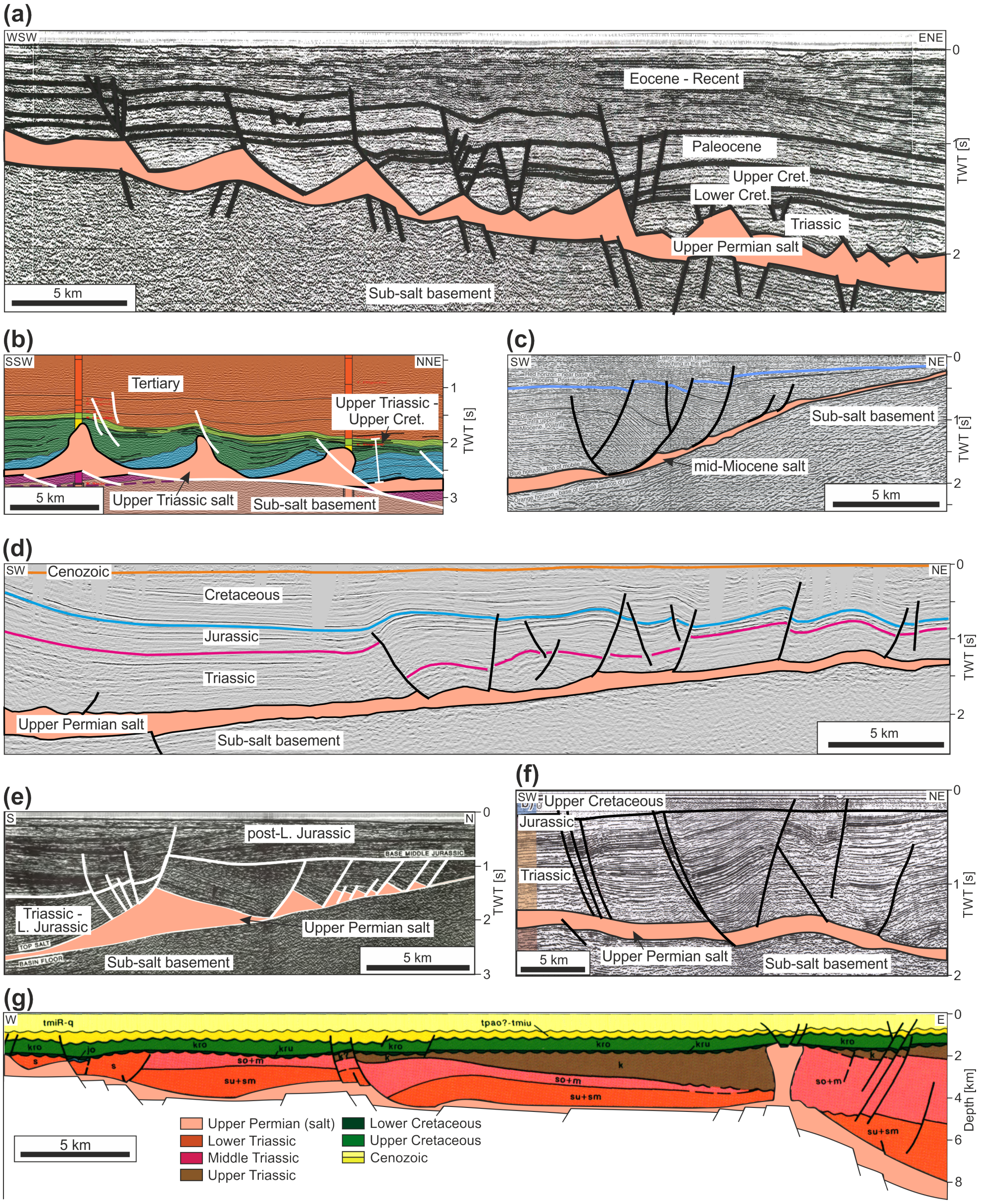

Figure 14. Examples of thin-skinned extensional structures recognized above inclined flanks at the margins of salt-bearing rift basins. (**a**) Northwestern Central Graben (North Sea): evenly spaced listric growth faults above a gently dipping, faulted sub-salt base (modified from Bishop et al., 1995). (**b**) Parentis Basin: tilted blocks and reactive diapirs of Upper Triassic salt (modified from Jammes et al., 2010). (**c**) Red Sea Basin: basinward dipping rollover faults above the mid-Miocene salt detachment (modified from Heaton et al., 1995). (**d**) Northeastern Polish Basin: peripheral extensional fault zones characterized by several supra-salt, tilted blocks and listric faults with increased thickness of Jurassic sediments. During the Late Cretaceous, the structure was inverted, and this inversion tectonic was associated with thin-skinned reverse faulting and folding (modified from Krzywiec, 2006b, 2012). (**e**) Norwegian-Danish Basin: triangular salt structures and tilted blocks overlie the inclined, unfaulted sub-salt base (modified from Geil, 1991). (**f**) Sole Pit Basin: thin-skinned Triassic graben structures above the Permian salt detachment were attributed to gravity gliding into the bowl-shaped basin centre (modified from Stewart, 2007). (**g**) Horn Graben (southeastern North Sea): listric growth faults in the Triassic strata overlie a relatively flat sub-salt base and are detached from the major graben structure (modified from Baldschuhn et al., 2001).